YSOVAR: MID-INFRARED VARIABILITY OF YOUNG STELLAR OBJECTS AND THEIR DISKS IN THE CLUSTER IRAS 20050+2720

K. POPPENHAEGER[1,13], A. M. CODY[2], K. R. COVEY[3], H. M. GÜNTHER[4], L. A. HILLENBRAND[5],
P. PLAVCHAN[6], L. M. REBULL[7], J. R. STAUFFER[7], S. J. WOLK[1], C. ESPAILLAT[8], J. FORBRICH[9], R. A. GUTERMUTH[10],
J. L. HORA[1], M. MORALES-CALDERÓN[11], AND INSEOK SONG[12]

[1] Harvard-Smithsonian Center for Astrophysics, 60 Garden Street, Cambridge, MA 02138, USA
[2] NASA Ames Research Center, Moffett Field, CA 94035, USA
[3] Western Washington University, 516 High Street, Bellingham, WA 98225, USA
[4] Massachusetts Institute of Technology, Kavli Institute for Astrophysics and Space Research, 77 Massachusetts Avenue, Cambridge, MA 02139, USA
[5] Department of Astronomy, California Institute of Technology, Pasadena, CA 91125, USA
[6] Missouri State University, 901 S. National Avenue, Springfield, MO 65897, USA
[7] Spitzer Science Center/Caltech, 1200 E. California Boulevard, Pasadena, CA 91125, USA
[8] Boston University, 725 Commonwealth Avenue, Boston, MA 02215, USA
[9] University of Vienna, Department of Astrophysics, Türkenschanzstr. 17, A-1180, Vienna, Austria
[10] Dept. of Astronomy, University of Massachusetts, Amherst, MA 01003, USA
[11] Centro de Astrobiología (INTA-CSIC), ESAC Campus, P.O. Box 78, E-28691 Villanueva de la Canada, Spain
[12] Physics and Astronomy Department, University of Georgia, Athens, GA 30602–2451, USA
Received 2015 April 30; accepted 2015 July 13; published 2015 September 22

ABSTRACT

We present a time-variability study of young stellar objects (YSOs) in the cluster IRAS 20050+2720, performed at 3.6 and 4.5 μm with the *Spitzer Space Telescope*; this study is part of the Young Stellar Object VARiability (YSOVAR) project. We have collected light curves for 181 cluster members over 60 days. We find a high variability fraction among embedded cluster members of ca. 70%, whereas young stars without a detectable disk display variability less often (in ca. 50% of the cases) and with lower amplitudes. We detect periodic variability for 33 sources with periods primarily in the range of 2–6 days. Practically all embedded periodic sources display additional variability on top of their periodicity. Furthermore, we analyze the slopes of the tracks that our sources span in the color–magnitude diagram (CMD). We find that sources with long variability time scales tend to display CMD slopes that are at least partially influenced by accretion processes, while sources with short variability timescales tend to display extinction-dominated slopes. We find a tentative trend of X-ray detected cluster members to vary on longer timescales than the X-ray undetected members.

Key words: accretion, accretion disks – infrared: stars – protoplanetary disks – stars: pre-main sequence – stars: variables: general

Supporting material: machine-readable and VO tables

1. INTRODUCTION

Protoplanetary disks are the birthplaces of exoplanets. As a star forms from a contracting cloud of gas and dust, the rotational collapse causes parts of the material to form a protoplanetary disk around it. The disk material close to the young stellar object (YSO) accretes onto the YSO's surface along the stellar magnetic field lines. Due to the stellar radiation, the temperature of the disk decreases radially from the inner parts of the disk to the outer parts. There has been observational progress in studying the formation of exoplanets in situ through interferometric observations with high spatial resolution, for example with ALMA (e.g., Casassus et al. 2013; de Gregorio-Monsalvo et al. 2013; van der Marel et al. 2013; Pineda et al. 2014), CARMA (e.g., Eisner et al. 2008; Enoch et al. 2009; Isella et al. 2009, 2010), SMA (e.g., Andrews & Williams 2007; Jørgensen et al. 2007; Andrews et al. 2009, 2011; Brown et al. 2009), or PdBI (e.g., Piétu et al. 2006; Hughes et al. 2009). Such observations have been successful in resolving the protoplanetary disk to distances below 100 AU from the central star; a recent example is the successful imaging of ring structures in the protoplanetary disk of the young star HL Tau (ALMA Partnership et al. 2015). However, it is very challenging to spatially resolve the processes happening in the disk within a few AU of the host star. Our prime observational tool in the study of the inner and mid-disk is therefore the variation in brightness of the star–disk system caused by the disk or an interaction between the star and the disk, such as accretion of disk material onto the star.

Given the temperature profile of a protoplanetary disk, we can observe processes at the inner rim of the disk in the near-infrared (*J*, *H*, and *K* bands) since the inner edge of the disk is determined by the dust sublimation temperature of ~1500 K.[14] This temperature implies that the blackbody radiation from the inner part of the disk peaks around 1–2 μm. Observations in the mid-infrared from ~3 to 20 μm provide observational access to parts of the disk which display surface temperatures of a few hundred Kelvin, i.e., parts of the disk with semimajor axes around 0.5 AU.

Variability of YSOs has been apparent since the earliest observations; initially, the main focus was the stellar photosphere studied through optical observations (Joy 1942;

---

[13] NASA Sagan Fellow.

---

[14] The dust sublimation temperature depends on the grain species and the local density (Pollack et al. 1994); 1500 K is a typically assumed value for protoplanetary disks (Dullemond et al. 2007, p. 555), with some observations matching sublimation temperatures of 1000–1500 K (Monnier et al. 2005), while some models use slightly higher temperatures of 1800–2000 K (D'Alessio et al. 1998).

Rydgren et al. 1976; Bouvier et al. 1986; Vrba et al. 1986; Herbst et al. 1994). To study the inner rim of the disk, monitoring in the near-infrared (mostly *JHK*) bands has been used (Skrutskie et al. 1996; Carpenter et al. 2001; Makidon et al. 2004 for example). These studies showed that a very large fraction (⩾90%) of the YSOs are variable in the near-infrared, for example, as determined for Orion, the Chamaeleon I Molecular Cloud, and Cyg OB7 (Carpenter et al. 2001, 2002; Rice et al. 2012). Near-infrared variability was found to occur on multiple timescales (Cohen et al. 2004; Grankin et al. 2007; Alves de Oliveira & Casali 2008) and the fraction of YSOs detected to be variable was reported to grow when multi-year baselines are taken into account (Scholz 2012).

While optical and near-infrared variability have been well studied for YSOs, it was initially unclear how parts of the disk farther out from the YSO behave as they are thought to be more dynamically stable. Early mid-infrared observations suggested variability (see Rebull et al. 2011 for a review). Long-term monitoring in the mid-IR revealed that YSOs in the cluster IC1396A fall into two classes of periodic and aperiodic variability in the mid-IR (Morales-Calderón et al. 2009), and new AA Tau-like objects and eclipsing binaries were found with those mid-IR data in the ONC (Morales-Calderón et al. 2011, 2012). A large-scale observational effort to study these parts of disks was made by the Young Stellar Object VARiability (YSOVAR) project (Rebull et al. 2014). In the scope of the project, 12 young stellar clusters were observed in the mid-infrared with the *Spitzer Space Telescope* (Werner et al. 2004). The aim of the project is to compare variability properties and associated disk processes over a wide range of cluster ages. A recent comprehensive study by Cody et al. (2014) combined *Spitzer* data with simultaneous monitoring with *CoRoT* in the optical. They presented a detailed analysis of different light curve morphologies for YSOs in the cluster NGC 2264, for example "dippers" and "bursters," the former showing sudden downward dips in the light curves, interpreted as changes in extinction, the latter showing upward spikes interpreted as accretion events (Stauffer et al. 2014). Günther et al. (2014) have presented an analysis of YSOVAR data for the cluster Lynds 1688 showing that variability amplitudes are larger for the most embedded objects, and Wolk et al. (2015), have shown for the YSOVAR cluster GDD 12–15 that YSOs with X-ray detections show variability on longer timescales than those with no X-ray detection. Flaherty et al. (2013) found a correlation of infrared variability fraction with X-ray luminosity for class II sources in the cluster IC 348, possibly due to accretion-induced hot spots changing the dust sublimation radius of the inner disk.

This present work discusses data collected and results derived for one of the YSOVAR clusters, IRAS 20050+2720. In this paper, we will analyze the variability of the IRAS 20050+2720 members in the mid-infrared. Section 2 discusses the cluster IRAS 20050+2720, Section 3 describes the collected observations, Section 4 demonstrates how we classified the detected sources and the types of variability, Section 5 describes our results and discusses them in the context of disk processes, and Section 6 summarizes our findings.

2. THE YOUNG CLUSTER IRAS 20050+2720

IRAS 20050+2720 is a young stellar cluster in which no massive stars have been detected (see Günther et al. 2012 and their Figure 7). This means that the evolution of its YSOs and their disks is not significantly altered by ultraviolet (UV) irradiation; such a UV influence on disks has been predicted (Johnstone et al. 1998) and observed for other clusters that do host massive stars (Guarcello et al. 2007; Balog et al. 2007, 2013; Wright et al. 2012; Guarcello et al. 2013).

IRAS 20050+2720 is located in the Cygnus rift at a distance of 700 pc from the Sun (Wilking et al. 1989). Objects in the Cygnus region can have substantial errors in their kinematically derived distance estimates if their galactic longitudes are close to 90°, because the local Galactic arm, the Perseus arm, and the outer parts of the Galaxy are lined up in that direction (Schneider et al. 2006). However, IRAS 20050+2720 is located at a galactic longitude of ca. 66° where the Cygnus X region and the Cygnus rift can be distinguished from each other, and therefore its distance estimate is deemed to be reliable (Beltrán et al. 2008). The central region of IRAS 20050+2720 has been found to display several radio lobes, which are likely due to jets from protostellar objects (Bachiller et al. 1995; Codella et al. 1999; Beltrán et al. 2008).

IRAS 20050+2720 consists of two cluster cores; the main cluster is located to the west (cluster core W), and a smaller core to the east (cluster core E) has been identified by Günther et al. (2012). Our observations target the main cluster core W, and all references to IRAC 20050+2720 in the remainder of the paper refer to cluster core W.

A first classification of likely cluster members has been performed in the infrared by Chen et al. (1997). They identified ca. 100 sources with IR excesses. Gutermuth et al. (2009) revisited this cluster and used *Spitzer* cryo-era observations to identify a total of 177 YSOs. Günther et al. (2012) have performed additional optical and X-ray observations of the cluster and have identified ca. 300 cluster members, among them ca. 50 sources which are young stars without visible disks (weak-lined T Tauri stars). Those objects could only be classified and distinguished from older foreground stars through X-ray observations because young stars are brighter in X-rays than older stars.[15]

3. OBSERVATIONS

We obtained mid-infrared light curves of objects in IRAS 20050+2720 during the *Spitzer* warm mission (Storrie-Lombardi & Dodd 2010); these observations are our main focus in this work, and we describe those data in detail in Section 3.1. An in-depth presentation of the data reduction is given in Rebull et al. (2014); for the convenience of the reader, we summarize the most important points in Section 3.1. We supplement these *Spitzer* observations with the auxiliary observational data listed in Table 1. Data from *Chandra* were used in our source classification scheme and data from PAIRITEL were specifically reduced for this work; we describe the reduction of those data sets in Sections 3.2 and 3.3.

3.1. Spitzer Data

The central region of IRAS 20050+2720 was observed with *Spitzer* from 2010 June 12 to 2010 August 10, using the 3.6 μm and 4.5 μm channel (hereafter [3.6] and [4.5]) of the IRAC camera (Fazio et al. 2004). *Spitzer* is able to observe simultaneously in [3.6] and [4.5], but the fields of view are

---

[15] The X-ray to bolometric luminosity ratio of young stars is of the order of 10^{-3}–10^{-4}, while it is typically smaller than 10^{-6} for older stars.

Table 1
List of Data Sets Used in This Work

| Telescope	Band	Epoch	Reference
Spitzer IRAC cold mission	3.6/4.5/8.0/24 μm	2007	Gutermuth et al. (2009)
Spitzer IRAC warm mission	3.6/4.5 μm	2010	This work
2MASS	J H K$_s$	1997	Skrutskie et al. (2006)
PAIRITEL	J H K$_s$	2010–2012	This work
FLWO/KeplerCam	U B V R I	2009	Günther et al. (2012)
IPHAS	r i Hα	2003–2005	González-Solares et al. (2008)
Chandra ACIS-I	X-ray (0.25–12 keV)	2006, 2007	Günther et al. (2012)
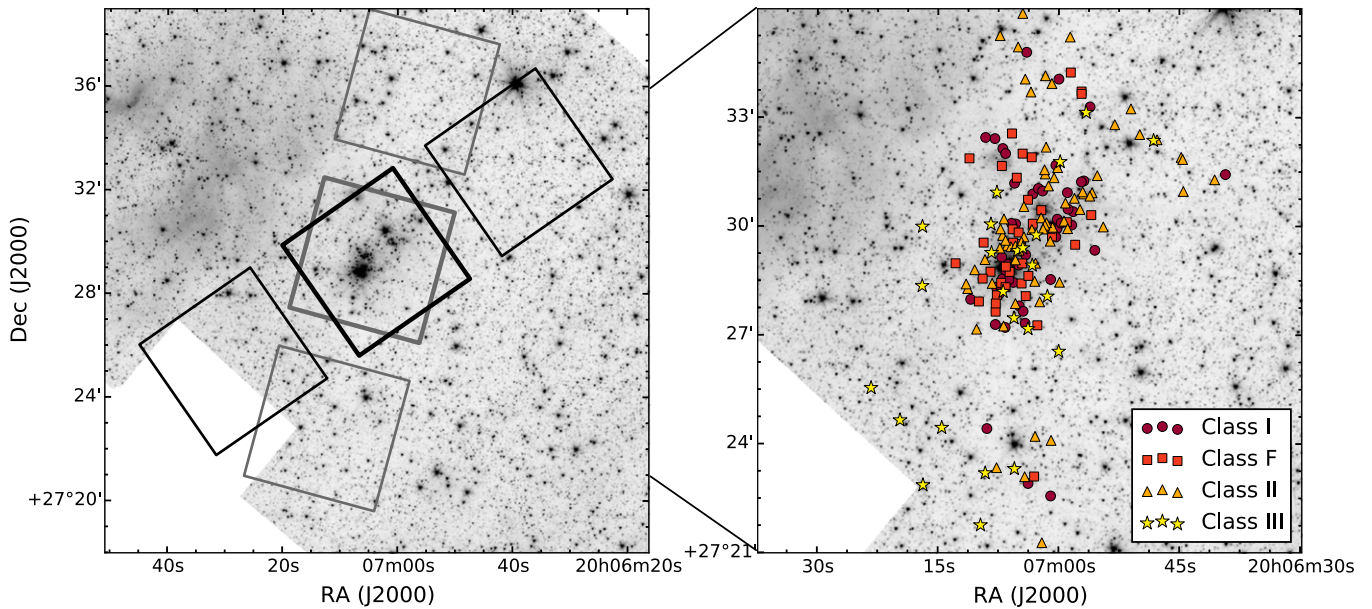
Figure 1. Left: fields of view of the *Spitzer* observations collected for IRAS 20050+2720, overlaid on a *Spitzer* 3.6 μm cryogenic-era image of the region. The field of view gradually rotated over the two months of observations, with sources inside the gray regions being observed at the start of the observing program and sources inside the black regions observed at the end. The middle field received coverage in both the [3.6] and [4.5] bands, while the upper fields were observed only in [3.6] and the lower fields in [4.5]. Right: zoomed-in image of the central field with the identified cluster members indicated.

adjacent and do not overlap. To obtain near-simultaneous light curves in both bands, the telescope first centers the [4.5] channel on the object, then the [3.6] channel, which results in a central area of the cluster which receives coverage in both [3.6] and [4.5], as well as two secondary areas which receive coverage in either [3.6] or [4.5]. We show a schematic representation of the fields of view in Figure 1.

The cadence of the observations was chosen to reduce aliasing when searching for periodic variability. We show a schematic representation of the observational cadence in Figure 2. It consists of a total of ca. 100 epochs with repeating sequences of increasing time steps in between them. Specifically, the time increments relative to a preceding epoch are roughly 4, 6, 8, 10, 12, 14, 16, and 18 hr. For the central field of view, which received coverage in both [3.6] and [4.5], the [3.6] pointings follow the [4.5] pointings with a time lag of ~2 minutes. Each individual observation was performed as an IRAC mapping mode Astronomical Observation Request using the high-dynamic-range (HDR) mode, which consists of a single 0.4 s and 10.4 s exposure.

3.1.1. Spitzer Data Processing

The photometry of the warm-era *Spitzer* observations was performed with the code *Cluster Grinder* (Gutermuth
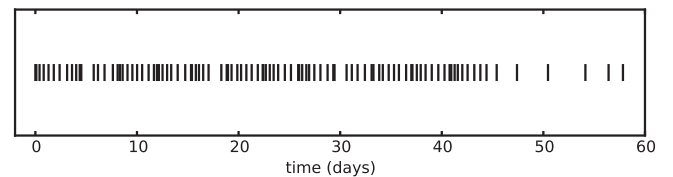
Figure 2. Time sampling of the *Spitzer* observations of IRAS 20050+2720, displayed for the full observational window of ca. 60 days. The time steps range from ~4 to ~18 hr for most of the light curve with some sparser time sampling every 2–3 days at the very end. The time lag between the [3.6] and [4.5] band is small in comparison (~2 minutes).

et al. 2009) written in Interactive Data Language (IDL). The starting point was the *Spitzer-Science-Center*-released basic calibrated data (BCD); the individual frames were combined into mosaics after processing for cosmic rays and bright source artifacts. Since the observations were performed in HDR mode, the two HDR exposures were combined into a single epoch by appropriately scaling the short-frame values for bright sources and replacing compromised pixels in the long frames.

For each epoch and channel we performed a point source detection and aperture photometry, using a source extraction radius of 2″.4 (2 pixels) and an annulus from 2″.4 to 7″.2 (6 pixels) for background estimation. Source matching of epochs and the two channels was performed by position with a

required cross-match radius of $\leqslant 1''$. The final position was taken to be the mean of the individual positions. A comparison with the 2MASS catalog (Skrutskie et al. 2006) shows uncertainties of <200 mas after a single global WCS cross-match to the catalog. A detailed discussion of the accuracy of the photometry and the associated noise floor is given in Rebull et al. (2014), Sections 2.5 and 2.6. The data used in this article will be delivered to the NASA/IPAC Infrared Science Archive (IRSA); it was retrieved from the YSOVAR database on 2014 September 10.

For the subsequent analysis of the light curves, we developed a set of Python routines named pYSOVAR (Günther & Poppenhaeger 2015) which are publicly available on github.[16] These routines calculate a set of statistical properties such as the mean, median, standard deviation, and maximum and minimum of the light curves, as well as more sophisticated quantities like autocorrelation timescales and a fit to the color–magnitude diagram (CMD) with data uncertainties on both axes.

3.2. Chandra Data

IRAS 20050+2720 was observed with the *Chandra X-ray Observatory* in three observations using the ACIS-I camera in VFAINT mode (ObsIDs 6438, 7254, 8492, PI Wolk). The exposure times and observation epochs were 21 ks (2006 January 07), 23 ks (2006 December 10), and 51 ks (2007 January 29), with a total exposure time of 93.95 ks, i.e., ~26 hr. The data reduction is described in detail in Günther et al. (2012); in short, the three exposures were merged, an automatic source detection was performed, and sources detected at a significance over 2σ were recorded. For sources with more than 20 X-ray counts a spectral fit was performed, using an optically thin thermal plasma model with a single temperature component with variable temperatue, absorbing column N_{H}, and emission measure. This work was performed in the context of a single-epoch IR study of IRAS 20050+2720 (Günther et al. 2012), and we use their derived X-ray properties here.

3.3. PAIRITEL Data

PAIRITEL is a 1.3 m robotic telescope operated by the Smithsonian Astrophysical Observatory on Mount Hopkins, AZ (Bloom et al. 2006); it was operational from 2004 to 2013. It was equipped with the JHK_s camera previously used for the 2MASS project. Photometric observations of IRAS 20050 +2720 were obtained during 31 nights between 2010 June 19 and 2012 July 10. We used Pyraf, a Python interface to IRAF (Image Reduction and Analysis Facility, Tody 1986), to perform the data reduction. The photometry was performed with the point-spread function (PSF) photometry tools of IRAF's DAOPHOT package (Stetson 1987). The observational frames were flat-fielded and bias-corrected. We then used `msccmatch` to match the world coordinate system of the PAIRITEL observations to the 2MASS catalog. We detected the source positions using `daofind` and performed the PSF photometry using tasks in the DAOPHOT package. The extracted instrumental magnitudes needed to be corrected for nightly extinction. We therefore matched the detected sources of each night to the 2MASS catalog, using a $1''$ matching radius, and performed a linear fit of the instrumental magnitudes to the 2MASS catalog magnitudes. This procedure

yielded calibrated JHK_s light curves for 341 sources; among the subset of sources that we will identify as cluster member in Section 4.1, we have collected 77 JHK_s light curves. The error bars of those photometric data points are often of a similar magnitude as the apparent variability, which is why we restrict ourselves in this work to only reporting the median JHK_s source magnitudes measured with PAIRITEL as listed in our data Table 2. The median magnitudes of the light curves agree well with the magnitudes in the 2MASS catalog (see Figure 3), with a standard deviation of 0.14/0.16/0.15 mag in the $J/H/K_s$ bands, respectively.

4. DATA CLASSIFICATION

4.1. Cluster Membership Criteria

In order to compare the properties of YSOs in the different young clusters of the YSOVAR project, we have selected a uniform system to identify likely members of these clusters. This system is based on an IR selection to identify YSOs with disks, as well as an additional X-ray selection to identify young disk-free stars.

We follow the IR selection by Gutermuth et al. (2009), who used cryogenic-era *Spitzer* data of the YSOVAR clusters to perform a multi-color selection of candidate members. This is thought to be a statistically well-defined sample with low contamination rates, as discussed in Gutermuth et al. (2008) and Gutermuth et al. (2009). We adopt all sources classified by Gutermuth et al. (2009) to have an IR excess (spectral energy distribution (SED) class I or II) as members.

Furthermore, we use X-ray observations of IRAS 20050+2720 to identify young diskless stars. We require an X-ray detection of at least 2σ significance and a positional match to a source identified in the cryo-era *Spitzer* catalog, as well as a star-like SED shape (see 4.2). The sources which fulfill these requirements are added to our list of members.

In the scope of the YSOVAR project we refer to a thus constructed list of members as the *standard set of members*. These are the sources for which we analyze mid-IR light curves in detail. Light curves of sources that are fainter than 16th magnitude in [3.6] or [4.5] are generally dominated by noise; they are usually prevented from entering the standard set because their SEDs are not well enough measured for them to have been identified as YSOs by Gutermuth et al. (2009). Since we are also mainly interested in time-variable processes here, we restrict ourselves to sources for which we actually have a light curve with at least five epochs in the post-cryogenic *Spitzer* data in either the [3.6] or [4.5] band. It is possible for a source to be a cluster member according to our definition, but have a light curve with too few data points to allow a useful analysis.

For our cluster IRAS 20050+2720, we have 187 sources that fulfill the membership criteria, and 181 of those have at least five data points in either their [3.6] or [4.5] band light curve. We will refer to those 181 sources as the standard set of members throughout this paper. In our data table (Table 2) they are marked with the flag "StandardSet." To identify the six sources that fulfill the membership criteria, but do not have light curves, we also list a flag "Member_without_LC" in Table 2. We summarize the numbers of cluster members in Table 3.

Recent publications on other YSOVAR clusters (Rebull et al. 2014; Günther et al. 2014) also analyze the statistical properties of all sources with light curves with at least five data

---

Table 2
Source Designations, Flux Densities, and Light Curve Properties

ID	Name	Unit	Channel	Comment
1	RA	deg	⋯	J2000.0 Right Ascension
2	DEC	deg	⋯	J2000.0 Declination
3	IAU_NAME	None	⋯	IAU designation within the YSOVAR program
4	simbad_MAIN_ID	None	⋯	Main identifier for an object
5	SEDclass	None	⋯	IR class according to SED slope
6	StandardSet	None	⋯	Source in YSOVAR standard set (cluster member with light curve)?
7	Member_without_LC	None	⋯	Is source cluster member without light curve?
8	n_36	ct	3.6 μm	Number of datapoints
9	n_45	ct	4.5 μm	Number of datapoints
10	median_36	mag	3.6 μm	Median magnitude
11	median_45	mag	4.5 μm	Median magnitude
12	mean_36	mag	3.6 μm	Mean magnitude
13	mean_45	mag	4.5 μm	Mean magnitude
14	min_36	mag	3.6 μm	Minimum magnitude in light curve
15	min_45	mag	4.5 μm	Minimum magnitude in light curve
16	max_36	mag	3.6 μm	Maximum magnitude in light curve
17	max_45	mag	4.5 μm	Maximum magnitude in light curve
18	delta_36	mag	3.6 μm	Width of distribution from 10% to 90%
19	delta_45	mag	4.5 μm	Width of distribution from 10% to 90%
20	LC_ok	None	⋯	Variability caused by light curve artifacts? (0: Yes, 1: No)
21	stetson_36_45	None	3.6 μm, 4.5 μm	Stetson index for a two-band light curve.
22	redchi2tomean_36	None	3.6 μm	Reduced χ^2 to mean
23	redchi2tomean_45	None	4.5 μm	Reduced χ^2 to mean
24	period	d	⋯	Adopted period of light curve
25	FAP	None	⋯	False alarm probability of adopted period
26	coherence_time_36	d	3.6 μm	Decay time of autocorrelation function
27	coherence_time_45	d	4.5 μm	Decay time of autocorrelation function
28	cmd_angle_360	degrees	3.6 μm, 4.5 μm	Fitted CMD slope angle in degrees
29	cmd_angle_error_360	degrees	3.6 μm, 4.5 μm	1σ error of fitted CMD slope angle
30	redchi2_phased_36	None	3.6 μm	Residual scatter in phase-folded fitted light curves
31	redchi2_phased_45	None	4.5 μm	Residual scatter in phase-folded fitted light curves
32	median_J	mag	J	Median PAIRITEL J band magnitude
33	median_H	mag	H	Median PAIRITEL H band magnitude
34	median_K	mag	K_S	Median PAIRITEL K_S band magnitude
35	Umag	mag	U	Günther et al. (2012) FLWO U band magnitude
36	e_Umag	mag	U	Statistical error in Umag
37	Bmag	mag	B	Günther et al. (2012) FLWO B band magnitude
38	e_Bmag	mag	B	Statistical error in Bmag
39	Vmag	mag	V	Günther et al. (2012) FLWO V band magnitude
40	e_Vmag	mag	V	Statistical error in Vmag
41	Rmag	mag	R	Günther et al. (2012) FLWO R band magnitude
42	e_Rmag	mag	R	Statistical error in Rmag
43	Imag	mag	I	Günther et al. (2012) FLWO I band magnitude
44	e_Imag	mag	I	Statistical error in Imag
45	Jmag	mag	J	2MASS J band magnitude
46	e_Jmag	mag	J	Statistical error in Jmag
47	Hmag	mag	H	2MASS H band magnitude
48	e_Hmag	mag	H	Statistical error in Hmag
49	Kmag	mag	K_S	2MASS K_S band magnitude
50	e_Kmag	mag	K_S	Statistical error in Kmag
51	3.6mag	mag	3.6 μm	Cryogenic *Spitzer*/IRAC 3.6 μm band magnitude
52	e_3.6mag	mag	3.6 μm	Statistical error in 3.6mag
53	4.5mag	mag	4.5 μm	Cryogenic *Spitzer*/IRAC 4.5 μm band magnitude
54	e_4.5mag	mag	4.5 μm	Statistical error in 4.5mag
55	5.8mag	mag	5.8 μm	Cryogenic *Spitzer*/IRAC 5.8 μm band magnitude
56	e_5.8mag	mag	5.8 μm	Statistical error in 5.8mag
57	8.0mag	mag	8.0 μm	Cryogenic *Spitzer*/IRAC 8.0 μm band magnitude
58	e_8.0mag	mag	8.0 μm	Statistical error in 8.0mag
59	24mag	mag	24 μm	Cryogenic *Spitzer*/MIPS 24 μm band magnitude
60	e_24mag	mag	24 μm	Statistical error in 24mag
61	FX	1e-7 ct cm^{-2} s^{-1}	X-ray	Günther et al. (2012) X-ray flux count rate

Note. This table is published in its entirety in the electronic verion of the journal. Here the table columns are described as a guide to form and content.

(This table is available in its entirety in machine-readable and Virtual Observatory (VO) forms.)
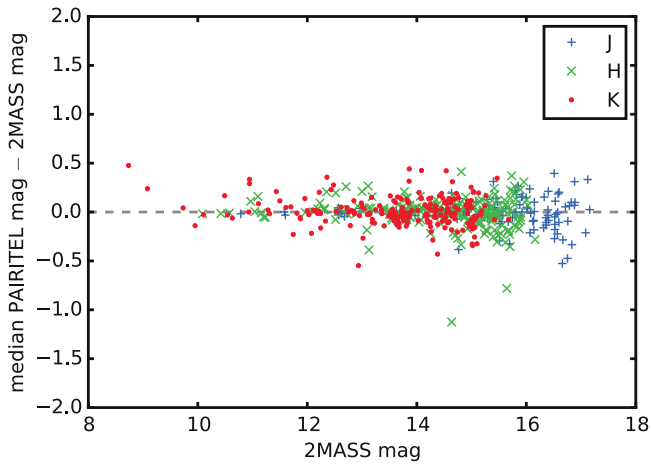
Figure 3. Sources in the field of view of the *Spitzer* observations of IRAS 20050+2720 for which PAIRITEL observations in *JHK_S* exist. The measured median PAIRITEL magnitudes for each source agree reasonably well with the magnitudes from the 2MASS catalog, with a typical standard deviation in the magnitude differences of ca. 0.15 mag.

Table 3
Numbers of Identified Cluster Members in IRAS 20050+2720

Type of Group	Number
Members	187
"Standard Set of members" (members with $\geqslant 5$ post-cryogenic light curve epochs)	181
Standard Set of members with two-band light curves	138
Standard Set of members with [3.6] light curve only	25
Standard Set of members with [4.5] light curve only	18
Additional X-ray identified candidate YSOs from Günther et al. (2012)	18

points, regardless of their cluster membership status. This group of sources is referred to as the *standard set for statistics*. In the present work, however, we restrict ourselves to the member sources, because especially in the cluster IRAS 20050+2720, the majority of the fainter sources are badly affected by image artifacts (see Section 4.3.4). For this reason, we defer a discussion of variables beyond the standard set of members to a later paper in the YSOVAR series that will compare variability properties across several clusters.

Apart from the standard set, we will also take a separate look at 18 additional sources identified by Günther et al. (2012). Those sources have not been detected in enough infrared bands to have a well-constrained SED, but they have been detected in X-rays and are all located close to the center of the cluster. Günther et al. (2012) call these objects "X-ray identified YSOs" ("XYSOs"), and we follow their nomenclature. Sources at the center of clusters are usually subject to strong extinction caused by the surrounding gas and dust and are therefore hard to detect in optical or infrared bands; however, X-rays can typically penetrate much larger column densities of absorbing gas. It is therefore not unusual to detect such sources at the cluster cores mainly in X-rays or in radio bands (Hughes 2001; Comito et al. 2007; Schneider et al. 2009; Pravdo et al. 2009). We have collected warm-era *Spitzer* light curves for 10 of these sources in IRAS 20050+2720, which we will discuss in Section 5.7.1.

4.2. SED Classification

During the different evolutionary stages of a YSO, its spectral energy distribution (SED) undergoes characteristic changes. Very young objects are still embedded in the envelope of gas and dust from which they are forming, and their SEDs peak at long wavelengths >10 μm (see, for example, Lada & Wilking 1984; Adams et al. 1987; Greene & Lada 1996). Objects with thick circumstellar disks will have an SED which is dominated by the flux at long wavelengths, while objects with thinner and dissolving disks will be dominated by the flux from the central object, but display NIR contributions from the disk emission. Once the disk is mostly dissipated, the SED is determined by the photosphere of the star.

We classify these SED slopes in a similar manner to Wilking et al. (2001), using the slope of the SED in the near- and mid-IR. Specifically, we use the data points from 2 to 24 μm as given in Gutermuth et al. (2008), add the means of the collected post-cryogenic *Spitzer* light curves at 3.6 and 4.5 μm as additional data points (i.e., in addition to the cryogenic-era 3.6 and 4.5 μm data points), and calculate the slope $\alpha = d \log \lambda F_\lambda / d \log \lambda$. The inclusion of a second epoch of [3.6] and [4.5] measurements reflects that our sources are expected to be variable; however, if only the cryogenic [3.6] and [4.5] data points are used, SED slopes generally do not change strongly enough to change the assigned class of a source. We refer to slopes with $\alpha > 0.3$ as Class I, $0.3 > \alpha > -0.3$ as Flat (F), $-0.3 > \alpha > -1.6$ as Class II, and $\alpha < -1.6$ as Class III. Details on this procedure are given in Rebull et al. (2014), Appendix B. As discussed there, fitting the observed SEDs (versus fitting de-reddened SEDs) is sufficient for our dataset, because we only fit SED data points redward of K_S. Substantial extinction of $A_V \sim 40$ would be needed to have a source be misclassified in our scenario.

Indeed, the overlap of our classification with the de-reddened classification scheme of Gutermuth et al. (2008) is satisfactory. We show a correspondence table between the two classification schemes for the members of IRAS 20050+2720 with at least five data points in their post-cryogenic *Spitzer* light curves in Table 4.

4.3. Variability Classification.

We investigate various types of time variability in the *Spitzer* [3.6] and [4.5] light curves of our sources. Typically, the standard set members have around 100 data points each in their [3.6] and [4.5] light curves; see Figure 4 for an overview. Sources that are positioned at the very edge of the *Spitzer* field of view tend to have $\leqslant 10$ light curve epochs. As listed in Table 3, 138 of the standard set members have light curves in both the [3.6] and [4.5] band, since the cluster core where most of the members are located was targeted by both IRAC channels. Twenty-five standard set members only have light curves in the [3.6] band; 18 only in the [4.5] band.

We test for three types of variability in our sample of mid-IR light curves: periodic variability, "χ^2-variability," and correlated variability if simultaneous light curves in more than one band are available. These methods are described in detail in Rebull et al. (2014); we give a short overview here and present typical cases of those variability behaviors.

Table 4
Assigned SED Classes of IRAS 20050+2720 Members with Light Curves (Down); Previously Assigned Classes from Gutermuth et al. (2008) Listed Across

	Class	Gutermuth						Sum
		I	I*	II	II*	III	Unclassified	
YSOVAR	I	35	6	6	0	0	0	47
	F	13	2	25	0	0	0	40
	II	1	0	65	4	0	0	70
	III	0	0	1	0	17	6	24
	Unclassified	0	0	0	0	0	0	0
	Sum	49	8	97	4	17	6	181
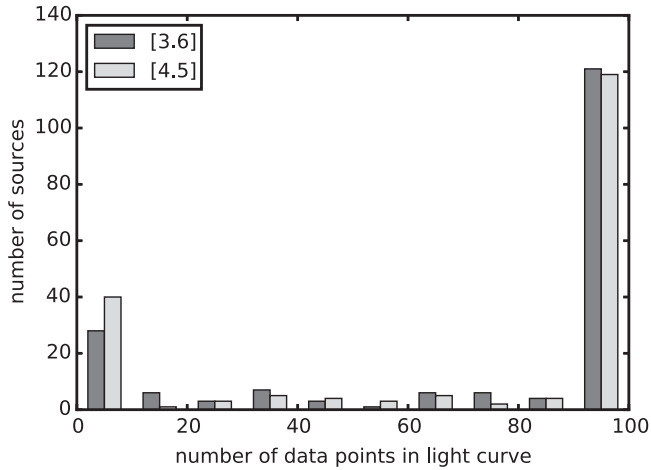
Figure 4. Number of sources in the standard set of members that contain a certain number of data points in the [3.6] and [4.5] light curves. Typically these light curves contain 100 data points each.

4.3.1. Chi-squared Variability Test

On any given light curve in our sample, we perform a chi-squared test for variability by calculating the reduced chi-squared statistic with respect to the mean for the time series:

$$\chi^2_{\rm red} = \frac{1}{N-1} \sum_{i=1}^{N} \frac{(\mathrm{mag}_i - \overline{\mathrm{mag}})^2}{\sigma_i^2} \qquad (1)$$

with N being the number of data points in the time series, mag_i the individual measured magnitudes, σ_i their individual errors, and $\overline{\mathrm{mag}}$ the mean of the measured magnitudes. As a conservative approach, we identify a source as χ^2-variable if its light curve in the 3.6 or 4.5 μm band yields $\chi^2_{\rm red} \geqslant 5$. As demonstrated by Rebull et al. (2014) in their Section 5.2, this corresponds to a significance larger than 3σ for source variability.

We show light curves of several sources that exceed this $\chi^2_{\rm red}$ variability threshold in Figure 5.

4.3.2. Correlated Variability

If simultaneous light curves in two bands are available, the Stetson index can be used as a measure for variability (Stetson 1996). It is calculated as

$$S = \frac{1}{N} \sum_{i=1}^{N} \mathrm{sgn}\left(P_i\right) \sqrt{|P_i|} \qquad (2)$$

with N being the number of paired observations in the two bands and $\mathrm{sgn}(P_i)$ is the sign of the quantity P_i. P_i, the product

of the normalized residuals for the ith two-band pair of observations is given by

$$P_i = \frac{N}{N-1} \frac{\mathrm{mag}_{i,[3.6]} - \overline{\mathrm{mag}_{[3.6]}}}{\sigma_{i,[3.6]}} \frac{\mathrm{mag}_{i,[4.5]} - \overline{\mathrm{mag}_{[4.5]}}}{\sigma_{i,[4.5]}}. \qquad (3)$$

A large positive Stetson index occurs for light curves in which correlated variability is present in both bands, while a negative Stetson index indicates anticorrelated behavior in the two bands. As shown by Rebull et al. (2014) in their Section 5.1, a value of $S > 0.9$ can be used as a robust indicator for variability of a given source. In addition, Rebull et al. (2014) showed in their Section 5.4 that the Stetson test is, as expected, generally more sensitive to variability features in YSOs than a one-band χ^2 test.

We show a set of sources with Stetson-variable light curves in Figure 6.

4.3.3. Periodic Variability

Finally, we test sources for periodic variability. Sources with low-amplitude periodic behavior may not be picked up by our (by design) conservative χ^2 threshold for variability, and they might fail the Stetson test for variability because the variability amplitude is too low or only single-band data is available. To search for periodic changes in unevenly spaced data, we decided to use the periodogram analysis provided by the NASA Exoplanet Archive Periodogram Service[17] (Akeson et al. 2013). Three different period search algorithms are provided by this service: Lomb–Scargle (Scargle 1982), box-fitting least squares (Kovács et al. 2002), and the Plavchan algorithm (Plavchan et al. 2008). They all have different strengths and weaknesses with repect to sinusoidal versus non-sinusoidal variations as well as periodic behavior on top of other light curve trends. After testing all three, the Lomb–Scargle approach turned out to be most suitable for our purposes; see the discussion in Rebull et al. (2014) for details.

For the period search, we require the light curve of a given source to contain at least 20 epochs. We ran a Lomb–Scargle period search for the 3.6 and 4.5 μm light curves, and, if both are available for the same source, also for the [3.6]–[4.5] color light curves. Because our total densely sampled epoch coverage is 40 days, we restricted our search to periods between 0.1 and 15 days and generally required a false alarm probability (FAP) of less than 0.03; for details see Rebull et al. (2014). Additionally, the phased light curves were checked by eye for consistency. If a

---

[17] http://exoplanetarchive.ipac.caltech.edu/cgi-bin/Periodogram/nph-simpleupload
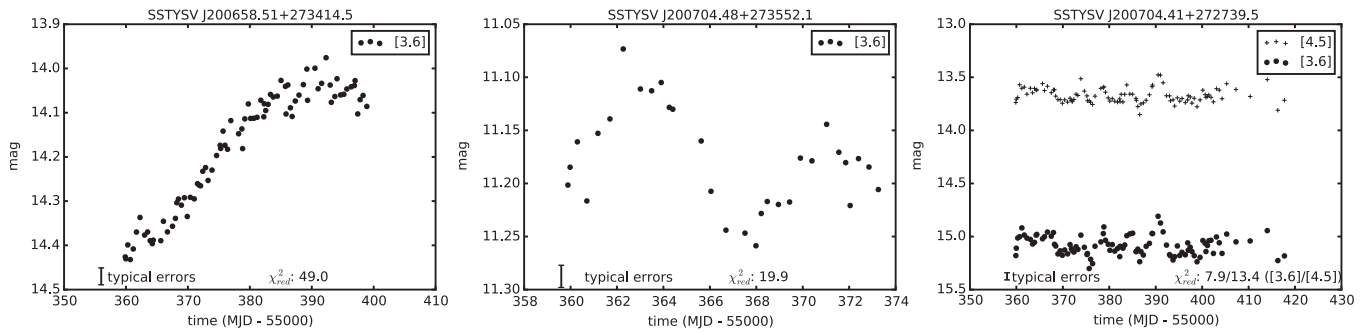
Figure 5. Examples of sources displaying χ^2 variability. Typical errors on the light curve data points and reduced χ^2 with respect to the mean of the light curve given at the bottom of each plot.
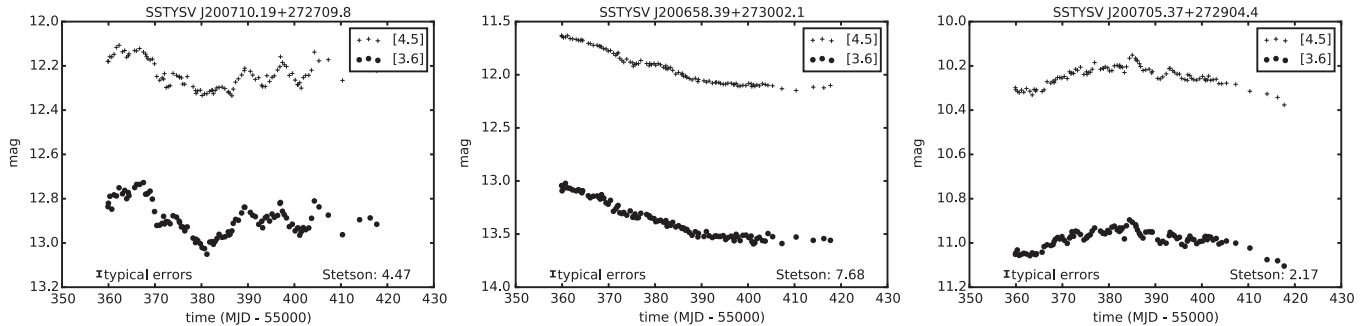
Figure 6. Examples of sources displaying correlated variability. Typical errors on the light curve data points and Stetson index given at the bottom of each plot.
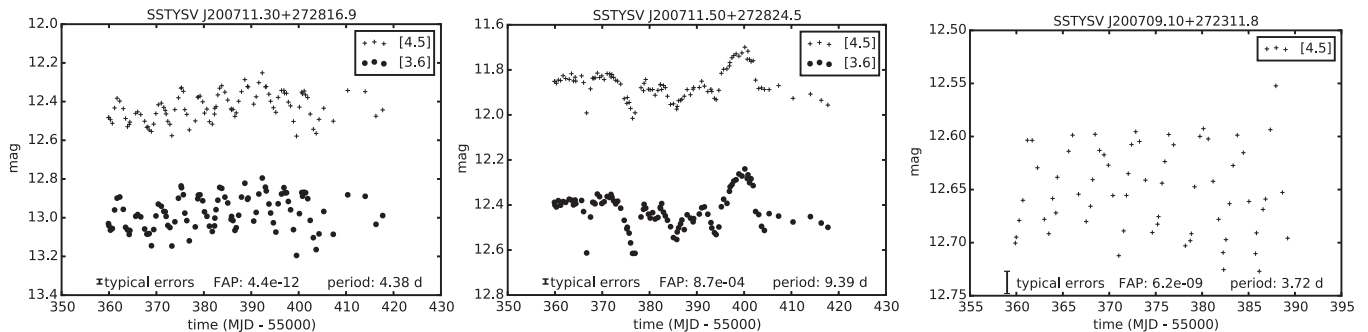
Figure 7. Examples of sources displaying a periodic signal in their variability; this can be overlaid by other, non-periodic signals like for the source in the middle plot. Typical errors on the light curve data points, false alarm probaility, and detected period given at the bottom of each plot.

significant period was detected, we gave preference to the period detected in the 3.6 μm band, because this band is generally less affected by long-term trends (such as changes in absorption by disk material in the line of sight); long-term trends make it hard for the Lomb–Scargle algorithm to identify underlying periods. If no significant period in 3.6 μm was detected, we proceeded as follows: if a significant period is detected in the 4.5 μm band, we report that period. If that band also does not show a significant periodicity, we test if the [3.6]–[4.5] color light curves show periodicity and report the period if it is significantly detected. In Table 2 we specify from which channel the reported period is derived. In total, we find 33 sources among the standard set members that display a significant periodicity. Twenty-one sources show periodicity in the [3.6] band. Out of those, 11 sources also show periodicity in the [4.5] band. An additional 9 sources show periodicity *only* in the [4.5] band. Eight sources show periodicity in the [3.6]–[4.5] color light curves, and among those there are three objects for which the periodicity is exclusively found in the color light curve.

We show light curves of several sources with detected periodic changes in Figure 7.

4.3.4. Spurious Variability Signatures

For the fainter stars, we found that some light curves in IRAS 20050+2720 display isolated variability features on the scale of a few days. It turned out that some of these features were produced by column pulldown effects of the IRAC arrays or by PSF artifacts of bright stars (which rotate with observation epoch) in the vicinity of the fainter source. We therefore visually checked all light curves and the images for such features and excluded sources with spurious variability from further light curve analysis.

As an example, we show in Figure 8 one source for which a spurious variability feature was produced by column pulldown induced by a bright source elsewhere on that column of the array. The number of cluster member stars for which we found such artifacts is fairly low among the bright sources, but a
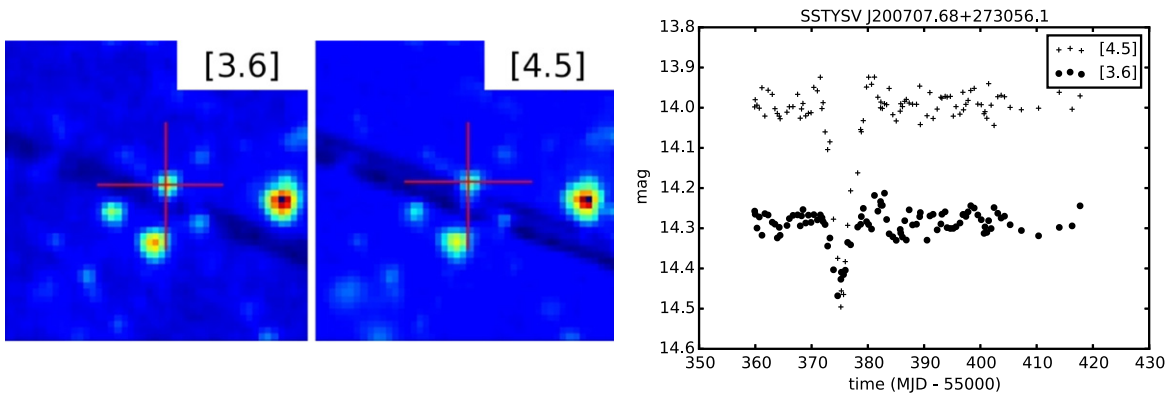
Figure 8. Example of a source with spurious variability in the light curve around MJD = 55 375, induced by column pulldown moving across the source due to the rotation of the field of view over time (see Section 2.5 in Rebull et al. 2014 for a detailed discussion of this instrumental effect).

larger fraction of the fainter sources was affected (see Figure 9). In total, out of 181 member stars with light curves, 26 objects were significantly affected and fully excluded from the variability analysis. In the following we will only refer to the 155 cluster members without light curve artifacts when discussing variability properties.

5. RESULTS AND DISCUSSION

5.1. Types of Variability and Detection Biases

We tested the standard set of members for variability of the types discussed above, i.e., χ^2, periodic, and Stetson two-band variability. We can compare the presence of variability signatures in different SED classes. However, the detectability of variability depends not only on the intrinsic source properties, but also on data coverage of that source, whether two-band data is available, and the apparent brightness of the source. A detailed analysis of our detectability thresholds for variable sources of different apparent brightness is given in Rebull et al. (2014). In addition, we mention here that Stetson indices could only be calculated for the middle field (see Figure 1), because this is the area where the fields of view of the [3.6] and [4.5] band observations overlap. The outer two fields were only covered in either [3.6] or [4.5], so that only single-band data is available for those. This skews the detection rates of correlated two-band variability for the SED classes, because the fraction of sources with SED classes II and III with available two-band light curves is slightly smaller than for the sources with SED classes I and F (see Table 5). This is an effect of class III sources being more spread out over the cluster and therefore being covered more often by the outward-lying one-band observation windows. Such differences in spatial extent have been observed in young stellar clusters before and are interpreted as an evolutionary effect due to movement of the older cluster members over time (e.g., Pillitteri et al. 2013).

In principle, we might also expect to see a skew in detectability for periodicity and χ^2-variability if the brightness of sources in the two observed *Spitzer* bands is very different by SED class. As shown in Figure 10, the brightness distribution peaks around 12–13 mag for all SED classes, with class III objects peaking at ca. 0.6 mag fainter than class II sources. We therefore expect a slightly smaller variability detection rate for class III objects based on IR brightness, but in general, differences in detected periodicity and χ^2-variability will mainly be driven by the amplitude and frequency of those variability types, i.e., by source-intrinsic properties.
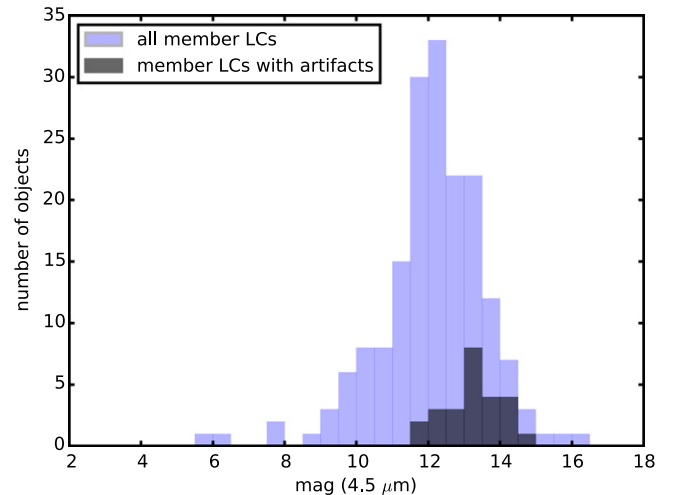

Figure 9. Brightness distribution of member sources with significant light curve artifacts (dark gray) vs. all member sources (light blue). As expected, mostly faint sources around $m[4.5] = 13$–14 mag are significantly affected by readout artifacts.

Table 5
Member Sources without Light Curve Artifacts with Two-band
Spitzer Light Curves, Split Up by SED Class

SED Class	# of Members	# of Two-band LCs	Fraction of Two-band LCs
I	43	35	$0.81^{+0.05}_{-0.06}$
F	33	29	$0.88^{+0.05}_{-0.06}$
II	59	38	$0.64^{+0.06}_{-0.06}$
III	20	11	$0.55^{+0.10}_{-0.11}$

5.2. Variability Fractions

We proceed by listing the number of detected variable member sources and specifying the variability type by SED class in Table 6. A graphical representation of the variability fractions is given in Figure 11, left. We find that 68% of all member sources with clean light curves (i.e., without artifacts) are detected to be variable with at least one type of variability. The overwhelming fraction of those are detected to be Stetson- or χ^2-variable. Note that this is not an exclusive identification; many sources are both Stetson- and χ^2-variable at the same time. In Figure 11, right, we show a Venn diagram in which the displayed areas approximate the overlapping numbers of
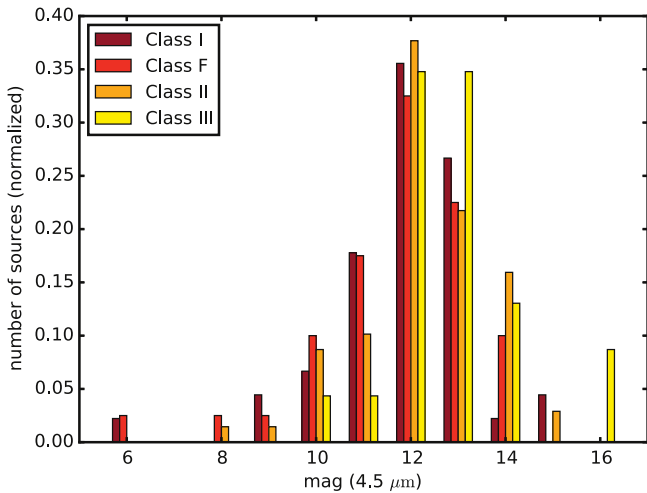
Figure 10. Brightness of member sources at 4.5 μm, split up by SED classes and binned in 1 mag intervals. Class III objects tend to be fainter, as expected for objects without disks compared to disk-bearing objects at the same distance.

sources and their variability type. We also note that we do not find any cluster members for which the [3.6] and [4.5] light curves are significantly Stetson-anticorrelated, as expected a priori.

Concerning the variability fractions and types in the individual SED classes of member sources, we find that the total variability fraction is around 70% for Class I, F, and II sources, with negligible differences. The overall variability fraction of Class III sources is lower with 45%. The strong drop in detected Stetson variability is real for class III sources, and not entirely due to the fact that a smaller fraction of class III sources have two-band light curves. If we calculate variability fractions only for objects with two-band data, we still find that about 70%–80% of class I, F, and II sources with two-band light curves display Stetson variability, but only ca. 9% of the class III sources with two-band light curves do. We will see in the next section that this is because the variability amplitudes are much smaller for class III sources, and therefore go mostly undetected except for periodic signals which are easier to pick out of the noise.

We find that the fraction of detected periodic variability is much lower for the disk-bearing sources, i.e., class I, F, and II objects, than the fraction of detected Stetson or chi-squared variability for the same group of sources. In contrast, most of the variable class III sources display periodic variability. This is due to the fact that the periodic signals are typically caused by starspots, which induce rather small modulation amplitudes at the observed wavelengths; other processes with larger amplitudes, such as disk changes or accretion signatures which take place in disk-bearing objects, often dominate the light curve so that small periodic signals are typically not picked up by the search algorithm. The disk-free objects, on the other hand, lack such large-amplitude processes, as shown in the next section, so that periodic signals are more readily detected. We will also give a more detailed discussion on the different physical processes causing variability in YSOs in Section 5.6. Our findings are consistent with the typically high variability fractions found in the mid-IR for other clusters. Morales-Calderón et al. (2011) reported a variability fraction of 70% among observed members of the ONC. Similarly, Flaherty et al. (2013) report a variability fraction of 60% for members of

IC 348. Cody et al. (2014) find ca. 90% of the members in NGC 2264 to be variable, Günther et al. (2014) report a variability fraction of ca. 80% for members of L1688, and Wolk et al. (2015), find comparable fractions of ca. 70% in GDD-1215.

5.3. Amplitudes of Variability

To characterize the amplitude of variability in a given light curve, we chose the spread of the individual magnitudes as an appropriate measure. To account for possible single outliers in the light curves, we report the 80% magnitude spread of a given light curve (i.e., the 90th percentile magnitude minus the 10th percentile magnitude). The result, broken up by SED class, is shown in Figure 12 for the two infrared bands, using all sources of the standard set of members that have been detected to be variable.

We find that sources with disks, i.e., SED classes I, F, and II, show a mean 3.6 μm variability amplitude of 0.19, 0.17, and 0.16 mag, respectively. The distribution is broad and reaches out to ca. 0.5 mag for disk-bearing sources. In contrast, diskless stars, i.e., objects with SED class III, show a markedly different variability amplitude pattern. They are preferentially detected with low variability amplitudes with a mean of 0.08 mag at 3.6 μm (compared to a typical standard deviation of 0.02 mag displayed by an individual light curve), and the histogram quickly falls off for larger amplitudes. We list the means of the variability amplitude distributions and the standard deviations of the respective distribution per SED class in Table 7.

To test if those distributions are drawn from the same parent distribution, we use the Anderson–Darling two-sample test (Anderson & Darling 1952; Scholz & Stephens 1987) for each of the possible combinations of two SED classes; this test is similar to a two-sample Kolmogorov–Smirnov test, but has a higher sensitivity to differences of the tails of the tested distributions. The result of this statistical test is given in the form of p values, i.e., the chance to obtain the observed difference in variability amplitudes, or a more extreme difference, if the parent distributions were in fact identical.

We find that the distribution of variability amplitudes is statistically indistinguishable for class I, F, and II sources, i.e., the sources with disks, whereas the disk-free class III sources show a distribution which is unlikely to be drawn from the same parent distribution as the class I and F sources ($p < 0.05$ for both the [3.6] and [4.5] band amplitudes).

The variability amplitudes we find for the IRAS 20050+2720 members are consistent with findings for other young stellar clusters. Günther et al. (2014) reported median [4.5] variability amplitudes of 0.26, 0.15, 0.14, and 0.05 mag for class I to III members of the cluster L1688; Wolk et al. (2015), find similar mean variability amplitudes of 0.17, 0.15, and 0.06 mag for class I, II, and III members of the cluster GGD12–15.

For several individual sources among the standard set of members, we find that the light curve spread in [3.6] tends to be larger than in [4.5], as seen in Figure 12, where many sources fall toward the [3.6] side of the diagonal line representing a 1:1 ratio. Generally, a larger spread in the [3.6] band is consistent with variability caused mainly by extinction. However, the difference in the light curve spread distributions turns out to be of low statistical significance for the sample of members in this cluster.

10

Table 6
Variability Fractions of Member Sources without Light Curve Artifacts by SED Class and Variability Type

Variability type	All Classes	Class I	Class F	Class II	Class III
Any kind	0.68 (105/155)	0.65 (28/43)	0.79 (26/33)	0.71 (42/59)	0.45 (9/20)
Periodic	0.18 (28/155)	0.16 (7/43)	0.03 (1/33)	0.20 (12/59)	0.40 (8/20)
Stetson	0.48 (75/155)	0.53 (23/43)	0.70 (23/33)	0.47 (28/59)	0.05 (1/20)
χ^2	0.59 (92/155)	0.63 (27/43)	0.73 (24/33)	0.63 (37/59)	0.20 (4/20)
Periodic & Stetson & χ^2	0.10 (15/155)	0.14 (6/43)	0.03 (1/33)	0.14 (8/59)	0.00 (0/20)
Periodic & Stetson, not χ^2	0.00 (0/155)	0.00 (0/43)	0.00 (0/33)	0.00 (0/59)	0.00 (0/20)
Periodic & χ^2, not Stetson	0.03 (5/155)	0.02 (1/43)	0.00 (0/33)	0.02 (1/59)	0.15 (3/20)
Periodic, not Stetson, not χ^2	0.05 (8/155)	0.00 (0/43)	0.00 (0/33)	0.05 (3/59)	0.25 (5/20)
Stetson, & χ^2, not periodic	0.35 (55/155)	0.37 (16/43)	0.61 (20/33)	0.31 (18/59)	0.05 (1/20)
Stetson, not periodic, not χ^2	0.03 (5/155)	0.02 (1/43)	0.06 (2/33)	0.03 (2/59)	0.00 (0/20)
χ^2, not periodic, not Stetson	0.11 (17/155)	0.09 (4/43)	0.09 (3/33)	0.17 (10/59)	0.00 (0/20)
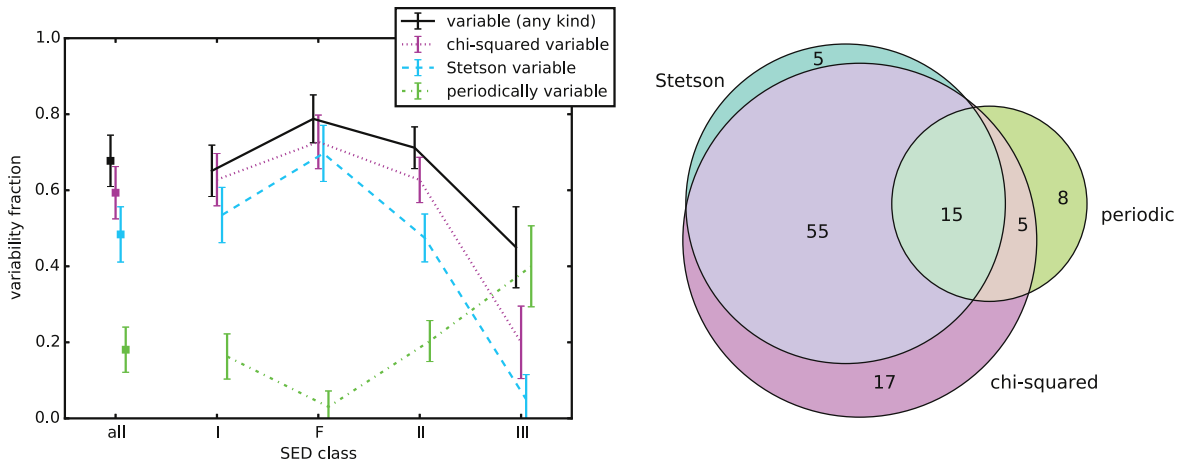
Figure 11. Left: fraction of variable sources in the standard set of members with light curves, split up by SED class and variability detection type. Right: Venn diagram (approx.) showing the overlap between different variability types for the standard set of members with light curves.

### 5.4. Timescales of Variability

Another quantity we want to test for SED-class specific behavior is the timescale of detected variability. In the case of periodic variation, this timescale is easily identified, namely as the detected period. However, the fraction of periodic sources in our sample of members is small ($<20\%$), as shown in Figure 11. We therefore chose to include sources with non-periodic variability in this timescale analysis.

For these sources, we use the coherence time of the autocorrelation function of the individual light curves as a time scale measure. The autocorrelation function, i.e., the cross-correlation of a time series with itself, can be used to test if some sort of recurring pattern is present in the time series. For periodic (or near-periodic) light curves, the autocorrelation displays one or more peaks at time lags corresponding to multiples of the period, and this has been used to infer stellar rotation periods, for example McQuillan et al. (2014). However, since we are also interested in phenomena that are not necessarily periodic (as we would have picked those up in our periodicity search already), we use the coherence time of the autocorrelation function as a measure for the characteristic time scale of changes in a light curve. As our time sampling is uneven and the autocorrelation function requires an evenly sampled input by definition, we linearly interpolated the light curves on time steps of 0.1 day. In principle, such an interpolation can change the variability properties of a light

curve; however, since we are looking for variability signatures on much larger time scales than 0.1 day, this is not an issue here. For a discussion of other timescale metrics that do not use linear interpolation, see Findeisen et al. (2015).

The coherence time refers to the time lag at which the autocorrelation function falls below a set value between 1 and −1 for the first time. This value is often chosen to be 0.5, but this is not optimal for the rather sparse time sampling of our light curves. This is due to the fact that the coherence time scales for our sources are rather short (of the order of a 0.5–1 days if using a threshold of 0.5), and that means that there are only very few steps necessary for the autocorrelation function to fall below the threshold, making it vulnerable to the effects of noise. We found that using a threshold of 0.25 for the autocorrelation function yields more robust results for our data.

In any case, the coherence time is not the characteristic time scale for changes in the light curve itself; it is a relative measure, i.e., a light curve with a shorter coherence time shows changes on a shorter timescale than a different light curve with a longer coherence time. As an example, we show a single light curve of a member source and its autocorrelation function, coherence time and actual timescale on which changes occur in Figure 13. As discussed in more detail by Wolk et al. (2015), one can show for sources where a periodical variation is detected that the coherence time and the detected period of the sources generally follow a linear relationship for our targets,
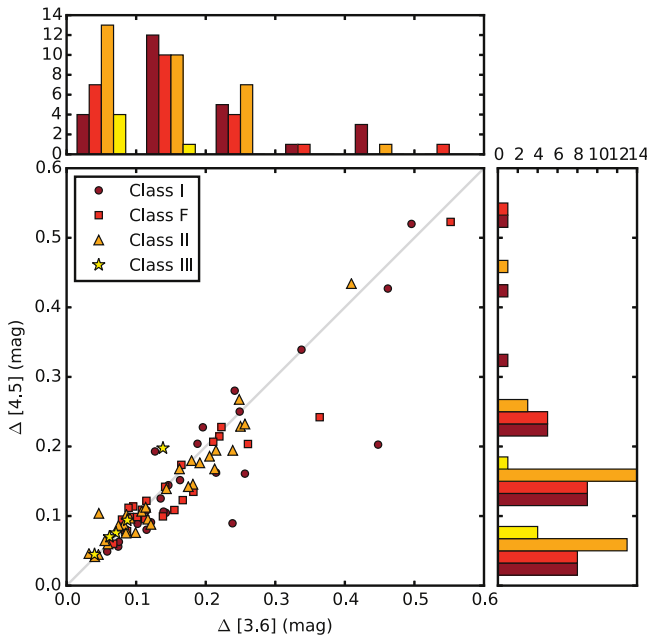
Figure 12. Amplitude of variability of light curves of cluster members (90th percentile minus 10th percentile in mag) in [3.6] and [4.5] is similar for SED classes I, F, and II, but significantly smaller for SED class III. The spread in flux of individual member star light curves tends to be larger in [3.6] than [4.5].

Table 7
Means and Standard Deviations of the Variability
Amplitude Distributions per SED Class

SED Class	Mean [3.6] ampl.(σ[3.6])	Mean [4.5] ampl.(σ[4.5])
Class I	0.19 mag (0.12 mag)	0.17 mag (0.11 mag)
Class F	0.17 mag (0.11 mag)	0.15 mag (0.09 mag)
Class II	0.16 mag (0.11 mag)	0.13 mag (0.08 mag)
Class III	0.08 mag (0.03 mag)	0.09 mag (0.05 mag)

with the period of a given source being ca. 3.5 times longer than the coherence time.

We next compare the detected periods and coherence times across SED classes for our cluster members, again using only sources without light curve artifacts. We give a graphical representation of the result in Figure 14, where the left plot shows the distribution of detected periods per SED class and the right plot shows the coherence times. As mentioned in Section 4.3.3, the [4.5] data often show longer-term trends overlaying the periodic short-term changes; since we are interested in the timescales dominating the behavior of a light curve, periodic or not, we focus on the coherence times in the [4.5] band here. However, as will be shown below, the results for the [3.6] band are qualitatively similar. For the periodic sources, we find preferentially periods between 2 and 6 days across all SED classes, with some longer periods >8 days detected for disk-bearing objects. The number of detected periodic sources is too small to test for differences in the distributions per class on a statistically significant level.

For the coherence times, we find that class I and II objects peak around 4 days with a significant tail to longer times; i.e., the actual time scales for light curve variability peak at $3.5 \times 4 = 14$ days. We have a smaller number of class F objects and their distribution is therefore more prone to sampling uncertainties; that aside, we find a peak at short

coherence times (<1 day) and a flatter peak around coherence times of 4–8 days. For disk-free class III sources, we find a noticeably different behavior with a strong peak at short coherence times <1 day and a steep decline toward longer coherence times. We list the means and standard deviations of the coherence time distributions per SED class in Table 8. We test if the distributions found for the different SED classes are compatible with being drawn from the same parent distribution, using the two-sided Anderson–Darling test. We find that nearly all pairings of coherence time distributions in two different SED classes are unlikely to stem from the same distribution ($p < 0.05$), except for the comparison between class I and class F in the [3.6] band and between class I and class II in the [4.5] band which do not pass this threshold.

### 5.5. Periodic Variability and Additional Scatter

For the 28 members of the standard set for which we have detected periodic variability, the noise in the phase-folded light curves differs strongly from source to source. In some of the cases, this is due to an underlying long-term trend; in other cases there seem to be additional short-timescale processes happening on top of the periodic variability. We show three examples of the original light curves and their phase-folded versions in Figure 15.

To quantify the presence and magnitude of processes on top of strictly periodic variability, we looked at the scatter in the original light curves with respect to the median compared to the scatter in the phase-folded light curves with respect to a fit to that light curve. Many of our sources do not display sinusoidal variations, but rather some complicated and often non-symmetric profile over the detected period. We therefore chose to fit the phase-folded light curve with a fifth-order polynomial, plotted with a gray line in the examples shown in Figure 15. The quantity we examine in the following paragraphs is the ratio of the reduced χ^2 values for the phase-folded light curves with respect to the polynomial fit, compared to the reduced χ^2 values of the original light curve with respect to the median.

Cody et al. (2014) used a slightly different approach to identify deviations from periodicity in *CoRoT* and *Spitzer* light curves in their Section 5.2. They remove long-term trends first, then subtract a smoothed version of the phased light curve, and finally evaluate the root mean square (rms) scatter of the residuals against the rms scatter of the original light curve. They label this ratio the "*Q* value." We have verified that the relationship of the two measurements of additional scatter (*Q* values and residual χ^2) is roughly linear for the sources where both quantities could be reasonably well determined. Given that we are dealing with significantly fewer data points in our light curves compared to optical *CoRoT* data, we adopt the approach described above.

We next compare the ratio of χ^2 values in the fitted phase-folded light curves and the original light curves (the scatter ratio) to two other quantities, namely the detected period and the peak-to-peak amplitude of the detected periodicity.

The scatter ratio versus period plot (Figure 16, top panel) shows a strong dependence on SED class. The amount of additional scatter on top of periodicity increases in the plot from the left to the right. We find that sources that are mostly periodic with low additional scatter (i.e., sources in the left half) are objects with SED class III or II, and display short periods of less than five days. Class III sources also extend into the right side of the plot, but stay at short periods. In contrast,
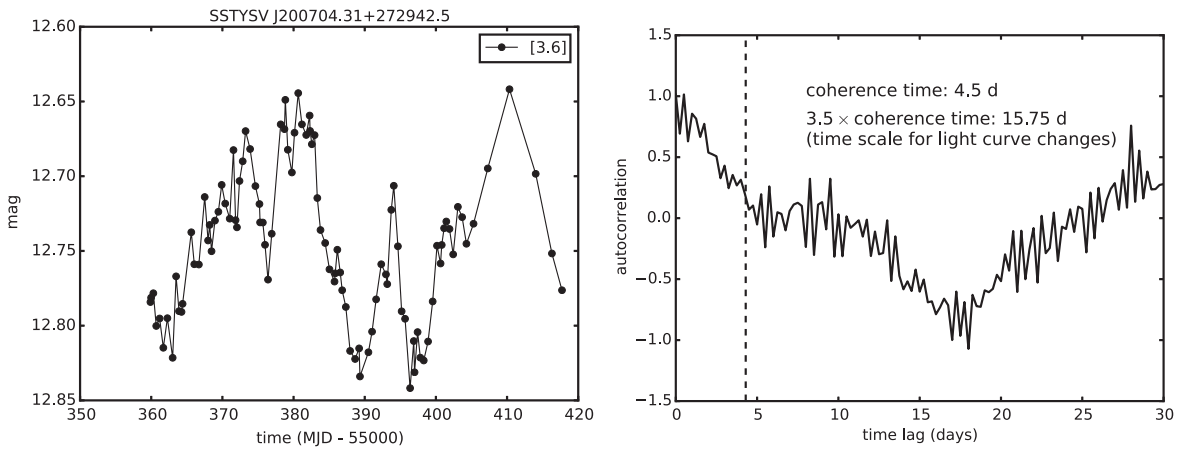
Figure 13. Light curve at 3.6 μm of a non-periodic source with SED class II (left) and the autocorrelation function of the light curve (right). The dashed vertical line represents where the autocorrelation falls below a value of 0.25 for the first time; we refer to this time scale as the coherence time.
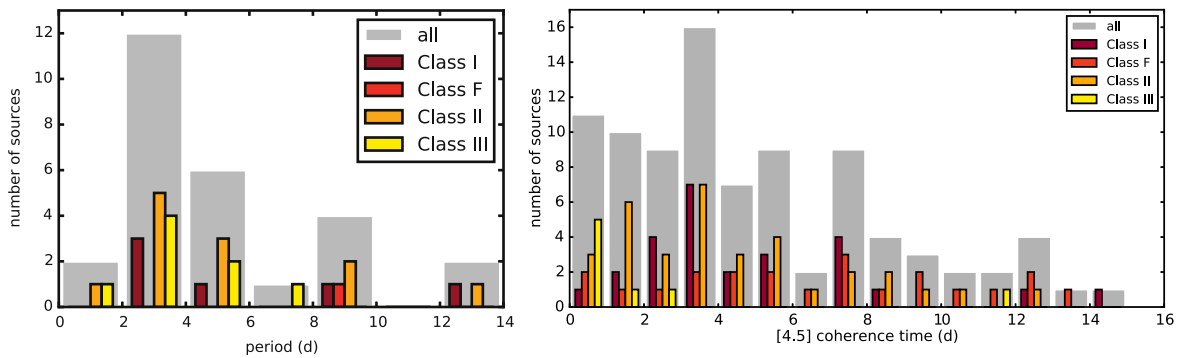
Figure 14. Distribution of detected periods (left) and detected coherence time scales in the 4.5 μm band (right) for member sources without light curve artifacts.

Table 8
Means and Standard Deviations of the Coherence Time t_{coh}
Distributions per SED Class

|	Mean [3.6] t_{coh} (σ[3.6])	Mean [4.5] t_{coh} (σ[4.5])
Class I	5.46 days (3.75 days)	4.97 days (3.30 days)
Class F	7.22 days (4.03 days)	7.50 days (4.49 days)
Class II	3.51 days (2.67 days)	4.36 days (2.90 days)
Class III	1.98 days (2.04 days)	2.41 days (3.41 days)

sources with disks, i.e., class II, F, and I, populate the full height of the right half of the plot, meaning that these sources can display large amounts of additional scatter at both short and long periods.

It is noteworthy that objects with SED classes I and F never display clean periodicity, but are always located on the right hand side of this plot.

It is in principle possible that this trend is caused by a peculiar distribution of amplitudes of periodic behavior across the SED classes. For example, if a source displays periodicity with a large amplitude and a small-amplitude extra scatter, the source will show up on the left side of the plot. However, if the periodic amplitude is smaller than the amplitude of the extra scatter, it will show up on the right-hand side. We therefore also looked at the extra scatter versus the peak-to-peak amplitude of the periodicity, inferred from the polynomial fit as shown in Figure 15. The result is shown in the bottom panel

of Figure 16. If the stratification in the top panel of Figure 16 was caused by different periodic amplitudes and not by differences in the additional scatter, we would expect to see sources with low scatter ratio to display high periodic amplitudes, i.e., to be located in the upper left, and sources with high scatter ratio to display low periodic amplitudes, i.e., be in the lower right. However, with the exception of two Class II sources which have moved significantly upward in this plot, the general distribution is the same as in the previous plot. Class III sources display low periodic amplitudes and little extra scatter, and Class I and F sources display high extra scatter, regardless of whether their periodic amplitudes are large or small. Class II sources populate both parts of the diagram.

This means that there is a true dependence of the "cleanliness" of periodic processes on the SED class of objects. This is not extremely surprising for Class III sources, since they have mostly lost their disks and should be dominated by periodic starspot modulations. We see that some Class II objects can mimic this behavior of periodicity without other apparent processes over the 40 day timescale of our observations. These Class II objects display short periods similar to the Class III sources; however, other Class II objects display high levels of additional scatter on top of the periodicity. It is noteworthy that *all* detected periodic Class I and F objects also have large additional scatter, and these objects display a wide range of periods. The additional scatter seems to be intrinsically linked to the presence of a disk; density fluctuations and
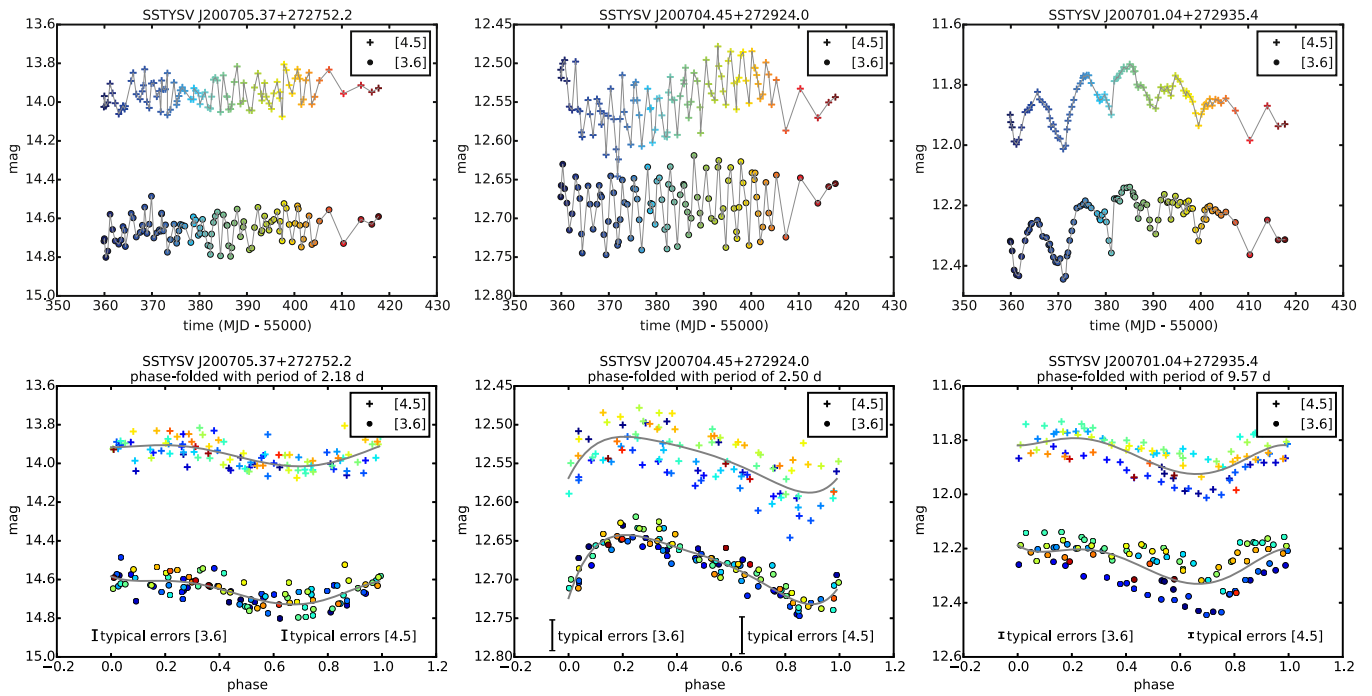
Figure 15. Three example sources with periodic variability; light curves in top panel, phase-folded light curves of the same sources in bottom panel. Color refers to time ordering (not phase ordering) of the data points in both panels. In the chosen examples, the amplitude of additional variability processes on top of the periodicity increases from left to right; the source in the middle shows long-term variability on top of the periodicity predominantly in the 3.6 μm band. The left and the right objects have SED class II, the middle object has SED class III.

fluctuations of the disk scale height may be explanations for this scatter.

5.6. Physical Processes Causing Variability: Clues from Color Space

Light curve morphologies can be a very useful tool to classify different types of behavior of young stars, as demonstrated by Cody et al. (2014). An additional dimension of color information comes into play if time-resolved photometry from more than one wavelength is available. In our case, we have the [3.6]–[4.5] color as a function of time as an additional parameter which we can investigate. Other colors derived from the *JHK* bands have been used for this purpose as well (Carpenter et al. 2001; Alves de Oliveira & Casali 2008; Wolk et al. 2013). Single-epoch color–magnitude diagrams (CMDs) in the near-infrared are also used to compare YSOs to stellar evolution isochrones and get a hande on the mass range of the objects in a cluster. This has been done for the members of IRAS 20050+2720 that have been detected in the *r'* and *i'* photometric bands (see Günther et al. 2012 and their Figure 7); these detected YSOs have masses below 3 $M_\odot$, the majority of them having masses between 0.2 $M_\odot$ and 1 $M_\odot$.

Different physical processes will cause different color changes over time. In Figure 17 we show the influence of cool spots, hot spots, gas and dust absorption, and an accretion model following Espaillat et al. (2010) on the [3.6] versus [3.6]–[4.5] CMD.

The slopes were derived as follows. For the spots, we assumed a stellar photospheric temperature of 5000 K, and cool and hot spots with temperatures of 4000 and 7000 K, respectively. For simplicity, we used a blackbody spectrum for the photosphere and spots. For illustrative purposes, we used large filling factors from 5% to 20% for both cool and hot spots.
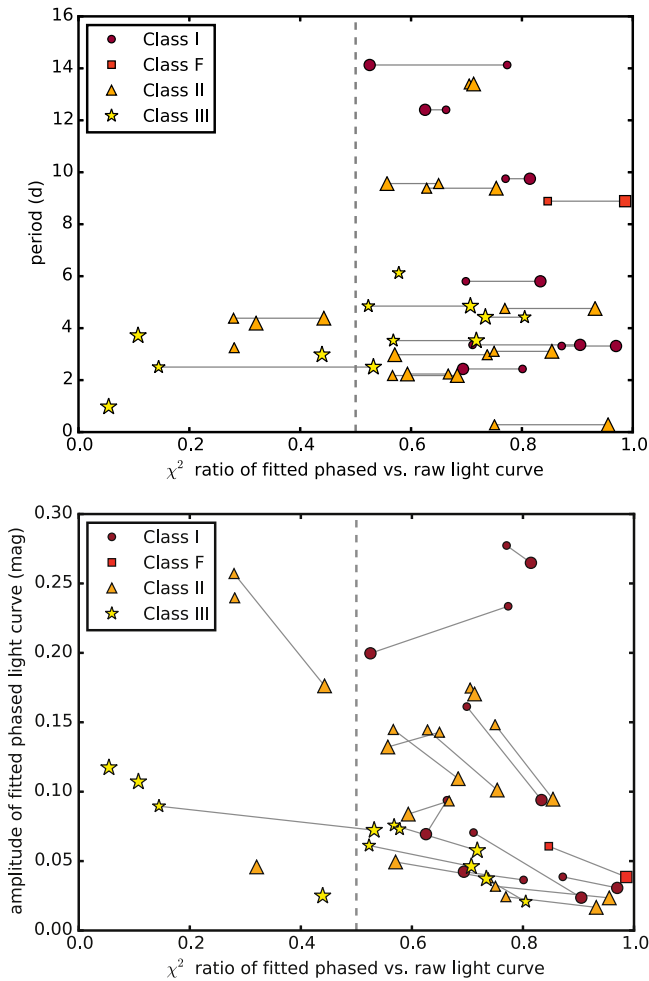
As can be seen from Figure 17, the changes due to spot coverage are almost vertical, i.e., colorless.[18] This is because we are far out in the Rayleigh–Jeans tail of the blackbody spectrum with the 3.6 and 4.5 μm bands. The predicted amplitudes of variability due to spots are relatively small for realistic spot coverages (ca. 0.15 mag or 15% in [3.6] and [4.5] for cool spots). The expected spot coverage fraction derived from actual observed modulations is much smaller than our illustrative values; in the near-infrared, where the induced modulation is stronger than in the mid-infrared, typical spot modulation amplitudes suggest spot coverage fractions of a few percent (Carpenter et al. 2001; Scholz et al. 2005; Wolk et al. 2013).

For extinction we show the typical effect of an ISM-like gas and dust mix on the CMD. Both the environmental density of gas and dust in the cluster and the material in the protoplanetary disk contribute to the extinction of our objects. However, since we observe short-term extinction events in our YSOVAR light curves those most likely caused by changes in the line of sight column density of the protoplanetary disk material. Because gas and dust absorb more strongly at shorter wavelengths, reddening of the spectrum occurs when the source gets fainter. The exact slope of the reddening depends on the gas-to-dust ratio of the extinction material, and on the grain size distribution of the dust. However, to give a general idea, we show the reddening vector measured for the ISM by Indebetouw et al. (2005).[19]

For the accretion effects a variety of models exist. Generally, accretion causes a redder color when the source gets brighter

---

[18] The resulting slopes for cool and hot spots modeled here are −14.6 and −14.2 in units of (−[3.6] mag)/(([4.5] − [3.6]) mag), i.e., steeply downward in a CMD where the brighter [3.6] mag are upwards on the *y* axis.
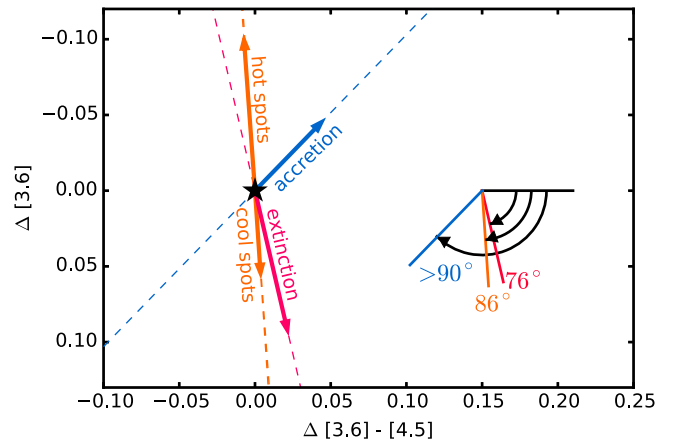
[19] The resulting extinction slope is −4.3 in units of (−[3.6] mag)/(([4.5] −[3.6]) mag).

Figure 17. Color–magnitude diagram (CMD) for IRAC's 3.6 μm and 4.5 μm bands. A given source (black star) will produce different walks through the CMD depending on the physical processes occurring. Increasing extinction by gas and dust, as well as surface coverage by hot or cool spots will cause walks that will make the source become redder when fainter and bluer when brighter, while increasing accretion in the plotted model will cause the source to become redder when brighter (and bluer when fainter for decreasing accretion). The specific models used for the tracks in this CMD are explained in the text. The direction in which we measure CMD angles is indicated by the schematic on the right hand side of the plot.
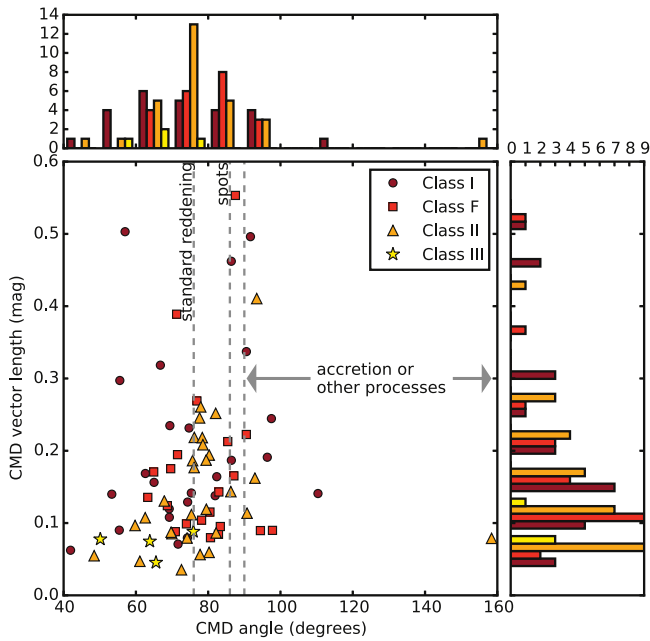
cause a source to become bluer as it gets fainter (see Bibo & The 1990 and Waters & Waelkens 1998 for examples of such behavior in UX Ori stars, and De Marchi et al. 2013 for a detailed geometric explanation for protoplanetary disks in general).

5.6.1. Color–Magnitude Slopes as a Function of SED Class and Variability

To investigate the dependence of CMD slopes on SED class, we performed linear fits to the CMDs of all sources in our standard set. We furthermore require that the sources do not possess light curve artifacts, and that they are flagged by our algorithm as variable sources (because if there is only statistical fluctuation in the light curves, the color slope is meaningless). The data points in the CMDs have non-negligible errors in both the x and y direction. To take these errors into account simultaneously, we performed a least-squares orthogonal fit to a straight line, using the python package scipy.odr which performs an Orthogonal Distance Regression with a Levenberg–Marquardt-type algorithm.[21] We define our slope angles as the clockwise angle from a horizontal line as shown in Figure 17. We show all fitted CMD slopes as a function of SED class in Figure 18, together with the length of the vectors spanned in the CMD (we use the 80% length spread to alleviate the effect of outliers). We have omitted sources with fitted slopes that have very large errors ($>10°$); typical errors are below 5°. The expected angular slopes for standard (ISM) reddening, cool and hot spots, and the general direction of accretion angles are indicated on the plot as well (76° for ISM reddening, 86°.2 for hot spots, 85°.8 for cool spots, and $>90°$ for other processes like accretion or scattered light). We find that only class I, F, and II sources display angles $>90°$ at all, as expected. The majority of those disk-bearing sources, however, show CMD slopes compatible with ISM reddening or spot

---

Figure 16. Top: the detected period vs. the scatter ratio (phase-folded and fitted light curve vs. raw light curve). SED classes of the objects are indicated by different symbols. The scatter ratios of a single source are generally different for the [3.6] and [4.5] band, and we show both in the plot, connected by gray lines. The value for the [4.5] band is indicated by the larger symbol. Sources in the left hand side of the plot show mainly periodic behavior with little extra scatter. Sources on the right hand side show large scatter remaining even after the periodic behavior is subtracted. Bottom: the peak-to-peak amplitude of the fit to the phase-folded light curve vs. the scatter ratio (phase-folded and fitted light curve vs. raw light curve). Again, data points for the same source in the [3.6] and [4.5] band are connected with gray lines. Apart from the two Class II sources in the upper left, we find the same population pattern as in the top panel, indicating that it is truly the amplitude of the additional scatter and not the amplitude of the periodic signal which drives the pattern in the top panel (see text for details).

and a bluer color when the source gets fainter. For illustration, we show a D'Alessio et al. (2006) disk model following Espaillat et al. (2010). In this model the effect of accretion is the formation of a hot spot on the stellar surface, which increases the irradiation of the disk. This additional flux heats the inner rim of the disk beyond the dust sublimation temperature, so that the inner hole of the disk widens and the surface temperature profile of the disk changes. With increasing mass accretion rates, a source seen at low inclination angles moves to the upper right of the CMD (sources seen edge-on will show deviations due to inclination effects).[20] However, there are other scenarios such as scattered light which may also

---

[20] The example of a possible accretion slope shown in Figure 17 is 1.2 in units of $(-[3.6] \text{ mag})/(([4.5] - [3.6]) \text{ mag})$.

[21] More details on the ODR package can be found here: http://docs.scipy.org/doc/scipy/reference/odr.html.

Figure 18. Distribution of CMD slope angles and length of the spanned vector in the CMD for the standard set of members. The majority of the sources show CMD angles compatible with extinction and spot modulation. Sources with large CMD angles caused by other processes such as accretion or scattered light tend to display longer CMD vectors.

Figure 19. CMD slope angle vs. coherence time in the 4.5 μm band. Cluster members with long coherence times (i.e., long-term light curve changes) tend to display CMD slopes bluer than ISM reddening.

modulation (or a combination of both). There are only four Class III sources with detected variability and a reasonably good fit to the CMD; this is because the variability amplitudes of the Class III objects are usually too small to yield a well-constrained CMD fit. The four variable Class III sources that do have non-negligible color changes display slopes that are significantly flatter than expected spot modulation. They are all detected to be periodic sources; they are also the sources that display significant additional scatter on top of their periodicity, i.e., sources in the lower right part of Figure 16.

In terms of the amplitude of variability in color space, i.e., the length of the spanned vector in the CMD, we find a dependence on SED class. Similar to the results for the overall variability amplitudes, we again find that class III sources span short vectors in the CMD, while the distribution of vector lengths for disk-bearing sources show a tail toward large CMD spreads; see Figure 18. This trend has also been reported by Wolk et al. (2015), for members of the cluster GDD12–15.

We find an interesting trend when we compare the CMD slopes with the time scales for variability of the sources, i.e., the periods and, for aperiodic sources, the coherence times. We find a trend of sources with longer variability time scales to display larger CMD slope angles as shown in Figure 19. The sample of periodic sources that have two-band light curves is too small to allow for a statistically significant result, but the sample of sources where we can calculate the coherence time scales is large enough to test for a correlation with CMD slopes. We use Spearman's rank correlation coefficient ρ for this; it is a non-parametric test (i.e., it does not assume a linear or otherwise specified shape of correlation). It spans values from -1 (perfect anticorrelation) to $+1$ (perfect correlation), with 0 meaning no correlation between the two variables. The significance of the correlation is again given by the corresponding p value, i.e., the probability that two random,
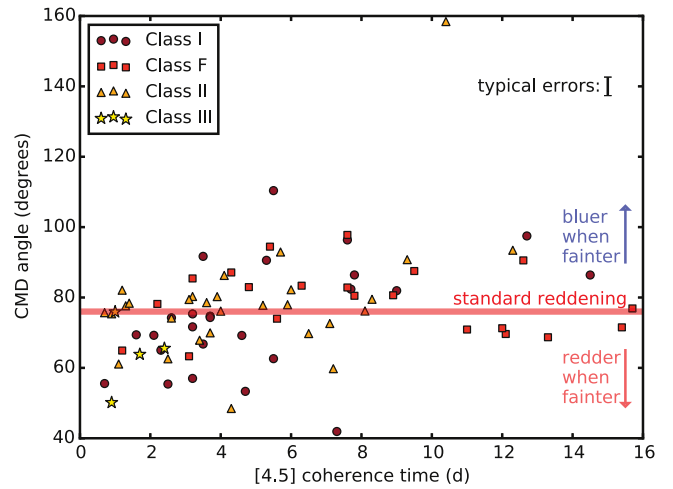
uncorrelated variables could show the same or a more extreme ρ value than the tested variables. Comparing the coherence time scales in each band and the CMD slopes of our member sources, we find a strong positive correlation of the slope with the [4.5] coherence time ($p = 0.00013$, $\rho = 0.42$) and with the [3.6] coherence time ($p = 0.015$, $\rho = 0.27$).

This means that changes in extinction and spot modulation tend to occur on longer time scales than changes in other processes like accretion that cause a blueing effect. Specifically, when blueing processes dominate the CMD, we find a mean [4.5] coherence time of 8.2 days (i.e., light curve changes typically occur on timescales of ca. 8.2×3.5 day $= 29$ day), whereas the mean [4.5] coherence time for sources with reddening is 5.1 days.

5.6.2. Examples for Processes in Color–Magnitude Space

A prime example where color information is crucial for the physical interpretation of the light curves is given in Figure 20, left and middle. It show two different sources, namely SSTYSV J200707.83+272738.8 (a Class F source) and SSTYSV J200700.17+273011.8 (a Class I source). These two sources have very similar light curve morphologies: The sources display low-amplitude variability for about 30 days, then a small increase in brightness, followed by a significant dimming of the order of 0.4 mag, lasting for ca. 20 days and then increasing slowly again. Despite these striking similarities, the CMDs display very different behavior. For the first source, the CMD is well-described by a straight line with a slope very close to the interstellar reddening law. A likely interpretation would be here that a blob of denser material in the disk has moved into the line of sight. Such dimmings were observed first for the eponymous YSO AA Tau, which displays extinction events by its disk on a semi-regular basis (Bouvier et al. 1999, 2013). The second source's CMD, however, shows that its data points are divided into two subclusters, and the slope between them is in the direction we expect for accretion events. Within the two subclusters, the individual slopes are roughly compatible with the ISM reddending vector again. Here the most likely interpretation is that a sudden drop in the accretion rate occurred which causes the dimming.

16
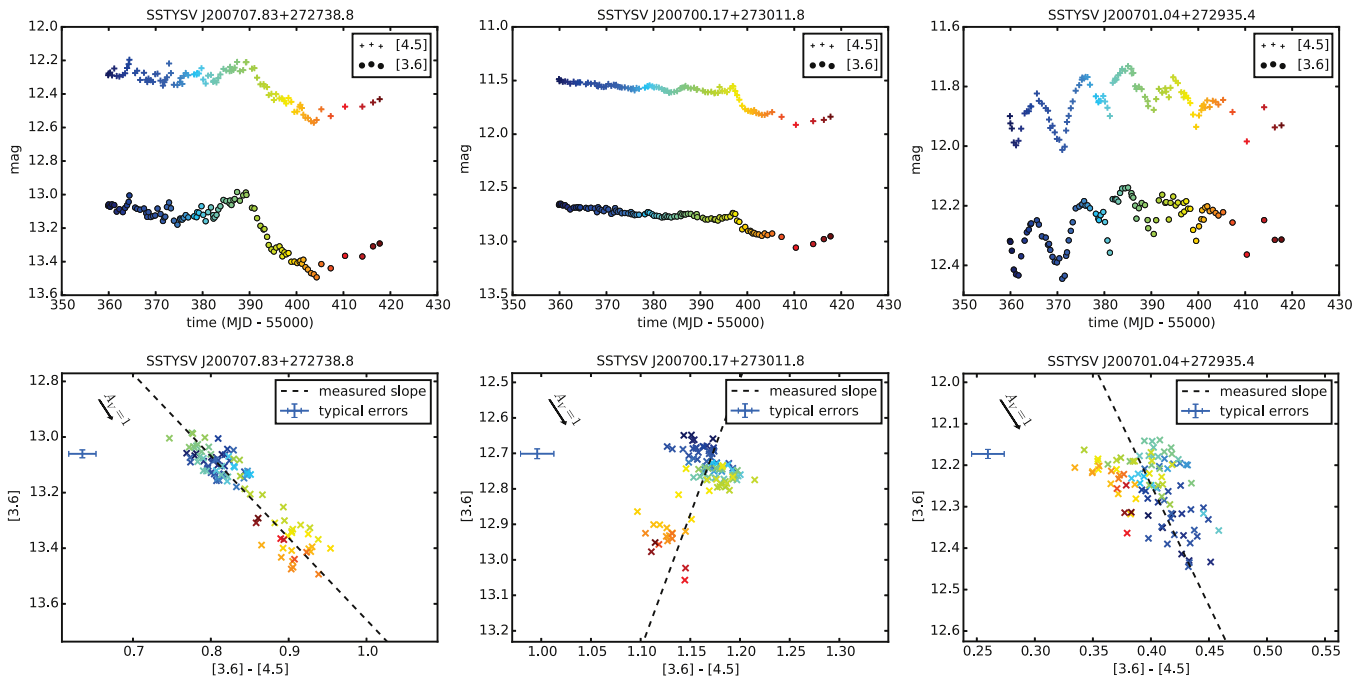
Figure 20. Examples of cluster members with distinct properties in the color–magnitude diagram (CMD). Light curves in top row, CMDs of the same source in the bottom row. Typical error bars are shown in the CMD plots. The X/Y ratio in these CMDs is different from the one in Figure 17 in order to make the slopes less steep and more easily visible; however, the X/Y ratios are the same in all CMDs in this figure and in Figure 21 to allow intra-source comparisons by eye. See text for discussion of individual sources.

The source SSTYSV J200701.04+272935.4 is what Cody et al. (2014) call a "dipper," i.e., it displays regular downward spikes in the light curve. This specific source is of SED class II, and its CMD shows a slope that is consistent with the interstellar reddening law. In addition, we can see a clustering by time in the CMD, indicated by the color coding in the plot in Figure 20, right. The data points in the CMD corresponding to times 400–420, indicated by orange/red crosses, are offset from the rest of the point cloud in a direction roughly orthogonal to the reddening vector. The data for this object generally supports the interpretation of Cody et al. (2014) that dippers are objects with (semi-) regular changes in extinction due to structures in their disk. In our example, this seems to be weakly overlaid with a gradual change in accretion as well, given the clustering of orange/red versus other data points in the CMD of this source.

Another example for a source with regular changes is SSTYSV J200703.21+273004.3, shown in Figure 21, left. While the source shows several brightening events, the change in time scales from one peak to the next and the additional upward slope prevent this source from being detected as periodic in our periodicity search. This "quasiperiodic" class F object shows a CMD slope perfectly in line with the interstellar reddening law by Indebetouw et al. (2005). As is evident in visual inspection of the CMD displayed in Figure 21, the scatter perpendicular to the reddening slope is not much wider than the typical photometric error on the color of this source. This means that both during the individual brightenings and the longer upward trend the brightness changes are dominated by extinction processes. This is consistent with small-scale structures in the disk causing time-variable extinction, as well as a slow decrease in density along the line of sight caused by larger-scale structural differences.

An interesting source with a high-amplitude brightening event is the class F source SSTYSV J200705.67+272932.9, shown in Figure 21, right. It displays an increase in brightness of 0.7 mag in both [3.6] and [4.5], with very small color changes. The overall CMD slope is formally consistent with what one would expect for hot or cool spots. However, the magnitude of the brightness changes is incompatible with that, as realistic spot coverage fractions yield a maximum of ca. 0.15 mag in [3.6] or [4.5] brightness as discussed above. The nature of this source's color changes can be interpreted as a mix of processes instead. The rise of the light curve (blue data points in the light curve and the CMD) is still consistent with a decrease in extinction along the line of sight. However, shortly before the peak is reached, the light curve displays a "knee" in the upward slope. This is where the CMD slope changes to much steeper, i.e., almost colorless track. A possible interpretation is that accretion set in at the knee of the light curve on top of the decreasing extinction; at the peak, the accretion begins to fade, and with a still ongoing decrease in extinction this could lead to the observed high-amplitude colorless change.

A total of 12 sources are present in our sample that have a blueing CMD slope, which we associate with accretion being the dominant variability process. Out of the 105 variable members that have two-color light curves and do not display light curve artifacts, this amounts to a fraction of 11%. These 12 sources are listed in Table 9; all of them have SED classes compatible with the presence of disks, as expected. Out of the blueing sources, all are detected to be Stetson-variable. Only a single source is flagged as periodically variable by our algorithm, the source SSTYSV J200702.00+273058.5. The fraction of blueing sources is consistent with the results of Günther et al. (2014) and Wolk et al. (2015), who both find
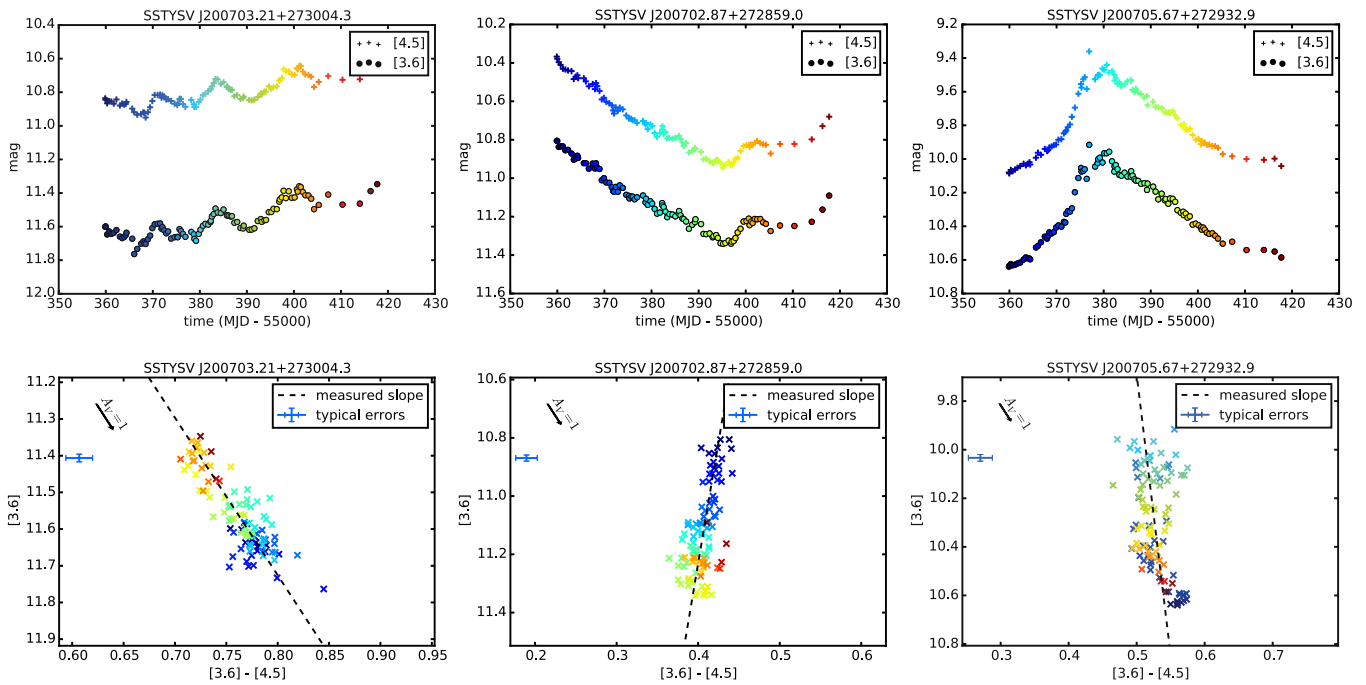
Figure 21. Like Figure 20, for three other sources.

Table 9
Sources in IRAS 20050+2720 that Show a Blueing CMD Slope

IAU Name of Source	SED Class
SSTYSV J200658.99+273006.9	F
SSTYSV J200706.59+272819.2	F
SSTYSV J200709.91+272755.6	F
SSTYSV J200700.17+273011.8	I
SSTYSV J200702.00+273058.5	I
SSTYSV J200706.60+273200.4	I
SSTYSV J200706.64+272712.7	I
SSTYSV J200707.85+272717.6	I
SSTYSV J200700.57+273120.4	II
SSTYSV J200702.87+272859.0	II
SSTYSV J200705.37+272904.4	II
SSTYSV J200706.83+272715.0	II

only a few blueing sources in their standard set of members for the clusters Lynds 1688 and GGD12–15, corresponding to a fraction of ca. 5%–15%.

Apart from the blueing source with the sudden drop in brightness that we already discussed above, another blueing source is particularly interesting: SSTYSV J200702.87 +272859.0, shown in Figure 21, middle. This source is a class II source, and it displays a substantial long-term dimming of 0.5 mag in both [3.6] and [4.5] over ca. 35 days. The slope of the CMD shows that the source is blueing when dimming, corresponding to a long-term change in accretion. Also the shorter episode at the end of the light curve where the source brightens in two steps seems to be governed by changing accretion, since the CMD does not show a sudden change of direction.

5.7. X-Rays and Infrared Variability

X-rays from young stars originate from magnetic activity of the stellar corona and from hot spots caused by accretion onto

the star. Strong X-ray flares are thought to be able to ionize and alter parts of the circumstellar disk; also, accretion from the disk onto the star has been found to produce an excess of soft X-ray emission through accretion shocks (for a review, see Günther 2013 and references therein). Therefore one may expect IR variability and the observed X-ray properties of the star to be correlated in some way. Recently, Flaherty et al. (2014) analyzed simultaneous X-ray and mid-IR light curves for members of the young stellar cluster IC 348 and found that X-ray variability and IR variability were not detectably correlated, which they interpreted as a sign that X-ray heating does not strongly influence the planet-forming part of the disk on time scales of a few days.

For our cluster IRAS 20050+2720, we do not have simultaneous X-ray and mid-IR light curves, and therefore resort to testing for general trends of mid-IR properties with X-ray brightness. Specifically, we will test if the X-ray detected and X-ray undetected cluster members show differences in their variability fractions, variability amplitudes, variability time scales, and slopes in the CMD. We will also test if these quantities show a trend with X-ray flux count rate within the X-ray detected sample.

We have detected a total of 67 sources in X-rays among the standard set of members (which is a total of 181 sources) using *Chandra* (see Section 3.2), with X-ray properties as given in Günther et al. (2012). Ignoring the objects with light curve artifacts, we have 58 X-ray detected, clean light curve objects among 155 standard set members with clean light curves. We want to compare the IR variability properties of the X-ray detected sample to the X-ray undetected sample. However, we have to be careful to consider systematic differences in IR brightness: the X-ray detected sources tend to be the least absorbed sources and are therefore on average IR-brighter than the X-ray undetected sources; see Figure 22. This means that we are able to detect IR variability with smaller amplitudes, and are therefore biased to find a larger variability fraction among
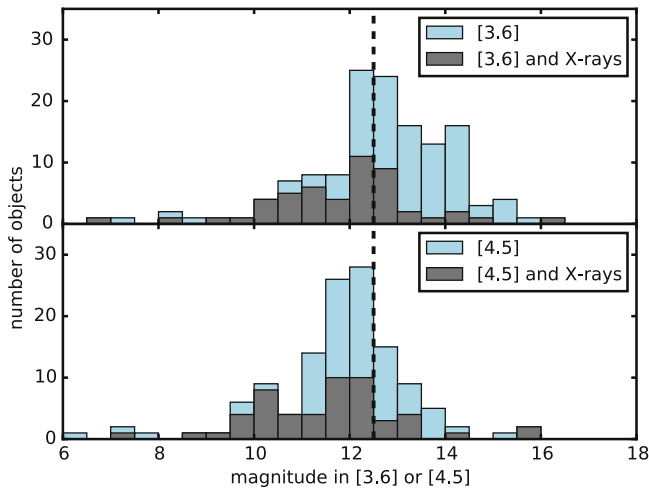
Figure 22. Distribution of [3.6] and [4.5] brightness of standard set cluster members (light blue); X-ray detected members (dark gray) tend to be bright in the infrared because they are the least absorbed sources. We therefore use a brightness cutoff at 12.5 mag (dashed line) for comparisons between X-ray detected and undetected members.

those bright sources. To counteract this bias, we have compared the [3.6] and [4.5] apparent brightness distribution of the X-ray detected and undetected samples, and found that cutting off sources with magnitude >12.5 in the [3.6] and [4.5] band yields a similar apparent brightness distribution for the two samples.

First, we investigated if the X-ray detected YSOs are more variable than the ones that are not detected in X-rays. We list the variability fractions per SED class for X-ray detected and undetected sources in Table 10. We find that within statistical error margins the fractions of IR-variable sources are the same among X-ray detected and undetected YSOs.

The quantity where we do find a significant trend with X-ray flux count rate is the variability amplitude in both IR bands. The distributions of variability amplitudes are statistically indistinguishable for the X-ray detected and undetected samples; however, in the X-ray detected sample, the variability amplitudes are strongly anticorrelated with the X-ray flux. We show this trend in Figure 23. A rank correlation test with Spearman's(s) ρ yields an anticorrelation with p values of 0.008 in [4.5] and 0.004 in [3.6], i.e., a very small chance that two uncorrelated samples would happen to show this or a more extreme anticorrelation. This is not driven by any systematic IR brightness trends within the X-ray detected sample, because both the X-ray flux count rate and the variability amplitude are uncorrelated with the median [3.6] and [4.5] brightness. Even when excluding the two sources with the largest infrared variability, we still find an anticorrelation with p values of 0.037 in [4.5] and 0.013 in [3.6].

The trend of sources with high X-ray flux count rates to have lower-amplitude mid-IR light curve changes therefore seems to be real. Note that in Figure 23 the sources with low-amplitude mid-IR variability populate both the low and high X-ray flux count rate parts of the plot, whereas the high-amplitude variables are only detected with low X-ray fluxes. This is not a direct effect of accretors being highly variable and X-ray bright: we only have two sources with blueing CMD slopes in the sample, marked with circles in Figure 23. A possible interpretation of the trend is that we are seeing an effect of the disk inclination—X-ray absorption is caused by heavier

elements in the gas phase of the disk, such as oxygen, nitrogen, and carbon. The mid-IR absorption, on the other hand, is mainly driven by dust particles. It is therefore possible that the sources with large detected X-ray fluxes are the sources we observe mostly face-on, so that the X-ray flux is not strongly absorbed. At the same time, extinction processes in the disk will not show up in the mid-IR light curves as well, because there is very little dust along the line of sight. Unfortunately, the large distance of IRAS 20050+2720 prevents a spectral X-ray analysis for many of the sources in this sample; one would expect to see absorption effects by gas from the disk on the soft part of the X-ray spectrum. An analysis of other, more nearby clusters has the potential to show if this X-ray brightness versus mid-IR variability trend can be used as a selector for disk inclination.

We furthermore test if other properties of the X-ray detected sample differ from the X-ray undetected sample, such as the color–magnitude slopes, the variability amplitudes or the time scales of variability. We do not find any significant differences in CMD slope distributions among the X-ray detected and undetected sources, nor a trend of the slope angles with the X-ray flux count rate in the X-ray detected sample alone. With respect to the coherence times, i.e., the timescales for variability, we find a slight trend of X-ray sources to have longer coherence times (using the magnitude-limited samples for comparison). However, an Anderson–Darling test between the two samples shows that two random samples drawn from the same distribution have a moderate chance to yield the same or a more extreme difference in coherence times; we find p values of 0.063 (0.019 for all sources with disks) in [4.5] and 0.18 (0.13 for all sources with disks) in [3.6]. Note however that Wolk et al. (2015), find this trend with higher significance for the YSOVAR cluster GDD1215; they are able to test for this difference on a larger sample of sources. In IRAS 20050 +2720, no significant correlations between the magnitude of the X-ray flux count rate and the coherence time are present in [3.6] or [4.5] within the X-ray detected sample.
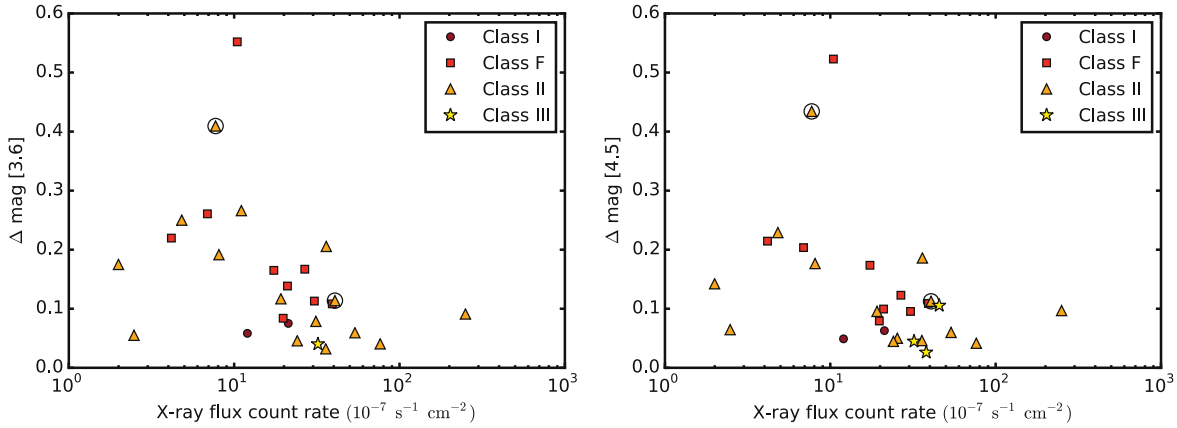
5.7.1. X-Ray Identified YSOs

IRAS 20050+2720 contains a number of sources near the center of the cluster that have not been classified by Gutermuth et al. (2009) because they have not been detected in enough bands to allow a reliable de-reddening. However, Günther et al. (2012) have detected these sources in X-rays and have listed them are likely cluster members which are obscured by high extinction of $A_V > 10$ mag and therefore only detected in a small number of infrared and optical bands. We have collected mid-IR light curves for 10 out of the thus identified 18 sources. We list their identities, our SED classes (which do not use a de-reddening scheme), and the median of the [3.6] and [4.5] *Spitzer* light curves in Table 11.

Two out of those sources are also listed in our standard set of members, because they are compatible with an SED class of type III and, by definition of being an XYSO ("X-ray identified YSO"), detected in X-rays. However, we list them here again together with the other XYSOs.

We find that three out of the 10 XYSOs with mid-IR light curves display light curve artifacts; out of the remaining seven, two are found to be variable. The variability fraction among those sources without artifacts is therefore $0.29^{+0.17}_{-0.13}$, which is slightly lower (at ca. 2σ level) than the variability fraction among the standard set of members of $0.68^{+0.04}_{-0.04}$. The lower

Table 10
Variability Fractions of IR-bright Member Sources, Comparison of X-Ray Sources to Full Sample

Type of YSO	All Classes	Class I	Class F	Class II	Class III
Variable among IR-bright	0.75 (52/69)	0.71 (10/14)	0.82 (14/17)	0.89 (25/28)	0.30 (3/10)
X-ray detected among IR-bright	0.57 (39/69)	0.14 (2/14)	0.59 (10/17)	0.64 (18/28)	0.90 (9/10)
Variable among X-ray detected and IR-bright	0.77 (30/39)	1.00 (2/2)	0.90 (9/10)	0.89 (16/18)	0.33 (3/9)

Figure 23. Variability amplitudes and the X-ray flux count rate are anticorrelated. The two YSOs that display a blueing CMD slope are marked with additional circles.

Table 11
X-Ray Identified YSO Candidates with *Spitzer* Light Curves in IRAS 20050+2720

IAU Name of Source	SED Class	LC Artifacts?	Median [3.6]	Median [4.5]	Variable?	CMD Slope Type
SSTYSV J200706.00+272901.7	I	yes	…	…	…	…
SSTYSV J200710.32+272853.8	I	no	16.02	15.09	no	…
SSTYSV J200708.20+272839.5	I	no	13.65	12.83	no	…
SSTYSV J200705.96+272910.1	F	no	…	11.98	no	…
SSTYSV J200707.90+272901.9	F	yes	…	…	…	…
SSTYSV J200707.31+272859.9	II	no	11.53	…	no	…
SSTYSV J200707.74+272852.5	II	yes	…	…	…	…
SSTYSV J200706.04+272856.6	II	no	9.62	…	no	…
SSTYSV J200705.11+272919.5	III	no	12.54	12.36	Stetson, χ^2	reddening
SSTYSV J200706.90+272812.0	III	no	13.78	13.38	periodic	reddening

variability fraction is not a bias induced by faint sources and therefore hard-to-detect variability, as all but one of the sources are relatively bright, see Table 11; this may be an indication that not all of the X-ray identified sources are actually YSOs. Among the sources with clean light curves in two bands and large enough variability amplitudes to fit the CMD slopes reliably, we find that they display reddening slopes throughout.

6. CONCLUSION

We have presented an analysis of mid-infrared light curves of 181 young stellar objects in the young cluster IRAS 20050 +2720. Our main findings are:

1. The variability fraction of sources with disks is high with 66%, 80%, and 73% for SED classes I, F, and II. Diskless class III sources are detected to be variable in 50% of the cases. While the overwhelming majority of the diskbearing sources are detected with irregular variability patterns, i.e., χ^2 or Stetson variability, the class III sources are mainly detected to be periodically variable, consistent with the interpretation that photospheric cool spots are the main driver of variability for these stars.

2. The detected amplitudes of variability are typically in the range of 0.14 mag for disk-bearing sources, with some sources displaying amplitudes of up to 0.55 mag in [3.6] and [4.5]. Disk-free sources show low-amplitude variability around 0.08 mag.

3. The time scales for variability tend to be longer for diskbearing sources, with a wide distribution out to 14 days for periodic sources. For non-periodic sources, we find through an analysis of coherence times that variability time scales reach out to 30 days in our dataset. For the disk-free sources, we find a strong clustering around shorter time scales of 3–5 days (periodic and nonperiodic), consistent with the scenario of stellar spin-up after the magnetic star-disk coupling interrupted by the dissolution of the circumstellar disk.

4. We analyzed periodic light curves for additional processes on top of the detected periodicity. We find that class I and F sources always display additional processes in our sample. Class II can display clean periodicity, but also strong additional variability signatures depending on the source. We generally find for disk-bearing sources that all objects with periods larger

than 8 days display a large amount of extra variability on top of the periodicity, whereas (disk-free) class III sources display clean periodicity.

5. We use CMD to distinguish between spots, extinction, and accretion as the dominant drivers of variability of a given source. We find that 10% of our sources with both [3.6] and [4.5] light curves show CMD slopes that turn bluer when fainter, consistent with accretion signatures during the time of the observations; however, other explanations like scattered light or unresolved binaries with brightness changes of one of the components are possible. We also find that sources with blueing slopes show variability on significantly longer timescales than sources compatible with variability by extinction or spot modulation.

6. We tested for different mid-IR variability properties among the cluster members that have been detected in X-rays. We find that the variability fraction is indistinguishable between the X-ray detected and undetected members, after controlling for different mid-IR brightness distributions of the sample. We find a weak trend of X-ray detected sources to display variability on longer time scales than their undetected counterparts. Among the X-ray detected members we find that their X-ray flux count rate and amplitude of mid-IR variability are anticorrelated, surprisingly. This may be an effect of disk inclination, causing X-ray absorption by gas in the YSO-disk system. The sources that are the most variable in the mid-IR may be the ones we are observing more edge-on.

7. All light curves will be made available through the IRSA database. The pYSOVAR code (Günther & Poppenhaeger 2015) used for the analysis of the light curves and CMDs is available through https://github.com/YSOVAR.

REFERENCES

Adams, F. C., Lada, C. J., & Shu, F. H. 1987, ApJ, 312, 788
Akeson, R. L., Chen, X., Ciardi, D., et al. 2013, PASP, 125, 989
ALMA Partnership 2015, arXiv:1503.02649
Alves de Oliveira, C., & Casali, M. 2008, A&A, 485, 155
Anderson, T. W., & Darling, D. A. 1952, Ann. Math. Statist., 23, 20
Andrews, S. M., & Williams, J. P. 2007, ApJ, 659, 705
Andrews, S. M., Wilner, D. J., Espaillat, C., et al. 2011, ApJ, 732, 42
Andrews, S. M., Wilner, D. J., Hughes, A. M., Qi, C., & Dullemond, C. P. 2009, ApJ, 700, 1502
Astropy Collaboration, Robitaille , T. P., Tollerud, E. J., et al. 2013, A&A, 558, A33
Bachiller, R., Fuente, A., & Tafalla, M. 1995, ApJL, 445, L51
Balog, Z., Muzerolle, J., Rieke, G. H., et al. 2007, ApJ, 660, 1532
Beltrán, M. T., Estalella, R., Girart, J. M., Ho, P. T. P., & Anglada, G. 2008, A&A, 481, 93
Bibo, E. A., & The, P. S. 1990, A&A, 236, 155
Bloom, J. S., Starr, D. L., Blake, C. H., Skrutskie, M. F., & Falco, E. E. 2006, ASP Conf. Ser. 351, Astronomical Data Analysis Software and Systems XV, ed. C. Gabriel et al. (San Francisco, CA: ASP), 751
Bouvier, J., Bertout, C., Benz, W., & Mayor, M. 1986, A&A, 165, 110
Bouvier, J., Chelli, A., Allain, S., et al. 1999, A&A, 349, 619
Bouvier, J., Grankin, K., Ellerbroek, L. E., Bouy, H., & Barrado, D. 2013, A&A, 557, A77
Brown, J. M., Blake, G. A., Qi, C., et al. 2009, ApJ, 704, 496
Carpenter, J. M., Hillenbrand, L. A., & Skrutskie, M. F. 2001, AJ, 121, 3160
Carpenter, J. M., Hillenbrand, L. A., Skrutskie, M. F., & Meyer, M. R. 2002, AJ, 124, 1001
Casassus, S., van der Plas, G., , M. S. P., et al. 2013, Natur, 493, 191
Chen, H., Tafalla, M., Greene, T. P., Myers, P. C., & Wilner, D. J. 1997, ApJ, 475, 163
Codella, C., Bachiller, R., & Reipurth, B. 1999, A&A, 343, 585
Cody, A. M., Stauffer, J., Baglin, A., et al. 2014, AJ, 147, 82
Cohen, R. E., Herbst, W., & Williams, E. C. 2004, AJ, 127, 1602
Comito, C., Schilke, P., Endesfelder, U., Jiménez-Serra, I., & Martín-Pintado, J. 2007, A&A, 469, 207
D'Alessio, P., Calvet, N., Hartmann, L., Franco-Hernández, R., & Servín, H. 2006, ApJ, 638, 314
D'Alessio, P., Cantö, J., Calvet, N., & Lizano, S. 1998, ApJ, 500, 411
de Gregorio-Monsalvo, I., Ménard, F., Dent, W., et al. 2013, A&A, 557, A133
De Marchi, G., Panagia, N., Guarcello, M. G., & Bonito, R. 2013, MNRAS, 435, 3058
Dullemond, C. P., Hollenbach, D., Kamp, I., & D'Alessio, P. 2007, Protostars and Planets V, ed. B. Reipurth, D. Jewitt, & K. Keil (Tucson, AZ: Univ. Arizona Press), 555
Eisner, J. A., Plambeck, R. L., Carpenter, J. M., et al. 2008, ApJ, 683, 304
Enoch, M. L., Corder, S., Dunham, M. M., & Duchêne, G. 2009, ApJ, 707, 103
Espaillat, C., D'Alessio, P., Hernández, J., et al. 2010, ApJ, 717, 441
Fazio, G. G., Hora, J. L., Allen, L. E., et al. 2004, ApJS, 154, 10
Findeisen, K., Cody, A. M., & Hillenbrand, L. 2015, ApJ, 798, 89
Flaherty, K. M., Muzerolle, J., Rieke, G., et al. 2013, AJ, 145, 66
Flaherty, K. M., Muzerolle, J., Wolk, S. J., et al. 2014, ApJ, 793, 2
González-Solares, E. A., Walton, N. A., Greimel, R., et al. 2008, MNRAS, 388, 89
Grankin, K. N., Melnikov, S. Y., Bouvier, J., Herbst, W., & Shevchenko, V. S. 2007, A&A, 461, 183
Greene, T. P., & Lada, C. J. 1996, AJ, 112, 2184
Guarcello, M. G., Drake, J. J., Wright, N. J., et al. 2013, ApJ, 773, 135
Guarcello, M. G., Prisinzano, L., Micela, G., et al. 2007, A&A, 462, 245
Günther, H. M. 2013, AN, 334, 67
Günther, H. M., Cody, A. M., Covey, K. R., et al. 2014, AJ, 148, 122
Günther, H. M., & Poppenhaeger, K. 2015, Astrophysics Source Code Library, record ascl: 1503.008
Günther, H. M., Wolk, S. J., Spitzbart, B., et al. 2012, AJ, 144, 101
Gutermuth, R. A., Megeath, S. T., Myers, P. C., et al. 2009, ApJS, 184, 18
Gutermuth, R. A., Myers, P. C., Megeath, S. T., et al. 2008, ApJ, 674, 336
Herbst, W., Herbst, D. K., Grossman, E. J., & Weinstein, D. 1994, AJ, 108, 1906
Hughes, A. M., Andrews, S. M., Espaillat, C., et al. 2009, ApJ, 698, 131
Hughes, V. A. 2001, ApJ, 563, 919
Indebetouw, R., Mathis, J. S., Babler, B. L., et al. 2005, ApJ, 619, 931
Isella, A., Carpenter, J. M., & Sargent, A. I. 2009, ApJ, 701, 260
Isella, A., Carpenter, J. M., & Sargent, A. I. 2010, ApJ, 714, 1746
Johnstone, D., Hollenbach, D., & Bally, J. 1998, ApJ, 499, 758
Jørgensen, J. K., Bourke, T. L., Myers, P. C., et al. 2007, ApJ, 659, 479
Joy, A. H. 1942, PASP, 54, 15
Kovács, G., Zucker, S., & Mazeh, T. 2002, A&A, 391, 369
Lada, C. J., & Wilking, B. A. 1984, ApJ, 287, 610
Makidon, R. B., Rebull, L. M., Strom, S. E., Adams, M. T., & Patten, B. M. 2004, AJ, 127, 2228

McQuillan, A., Mazeh, T., & Aigrain, S. 2014, ApJS, 211, 24
Monnier, J. D., Millan-Gabet, R., Billmeier, R., et al. 2005, ApJ, 624, 832
Morales-Calderón, M., Stauffer, J. R., Hillenbrand, L. A., et al. 2011, ApJ, 733, 50
Morales-Calderón, M., Stauffer, J. R., Rebull, L., et al. 2009, ApJ, 702, 1507
Morales-Calderón, M., Stauffer, J. R., Stassun, K. G., et al. 2012, ApJ, 753, 149
Ochsenbein, F., Bauer, P., & Marcout, J. 2000, A&AS, 143, 23
Piétu, V., Dutrey, A., Guilloteau, S., Chapillon, E., & Pety, J. 2006, A&A, 460, L43
Pillitteri, I., Wolk, S. J., Megeath, S. T., et al. 2013, ApJ, 768, 99
Pineda, J. E., Quanz, S. P., Meru, F., et al. 2014, ApJL, 788, L34
Plavchan, P., Jura, M., Kirkpatrick, J. D., Cutri, R. M., & Gallagher, S. C. 2008, ApJS, 175, 191
Pollack, J. B., Hollenbach, D., Beckwith, S., et al. 1994, ApJ, 421, 615
Pravdo, S. H., Tsuboi, Y., Uzawa, A., & Ezoe, Y. 2009, ApJ, 704, 1495
Rebull, L. M. 2011, in ASP Conf. Ser. 448, 16th Cambridge Workshop on Cool Stars, Stellar Systems, and the Sun, ed. C. Johns-Krull, M. K. Browning & A. A. West (San Francisco, CA: ASP), 5
Rebull, L. M., Cody, A. M., Covey, K. R., et al. 2014, AJ, 148, 92
Rice, T. S., Wolk, S. J., & Aspin, C. 2012, ApJ, 755, 65
Rydgren, A. E., Strom, S. E., & Strom, K. M. 1976, ApJS, 30, 307
Scargle, J. D. 1982, ApJ, 263, 835
Schneider, N., Bontemps, S., Simon, R., et al. 2006, A&A, 458, 855
Schneider, P. C., Günther, H. M., & Schmitt, J. H. M. M. 2009, A&A, 508, 321

Scholz, A. 2012, MNRAS, 420, 1495
Scholz, A., Eislöffel, J., & Froebrich, D. 2005, A&A, 438, 675
Scholz, F. W., & Stephens, M. A. 1987, J. Am. Stat. Assoc., 82, 7
Skrutskie, M. F., Cutri, R. M., Stiening, R., et al. 2006, AJ, 131, 1163
Skrutskie, M. F., Meyer, M. R., Whalen, D., & Hamilton, C. 1996, AJ, 112, 2168
Stauffer, J., Cody, A. M., Baglin, A., et al. 2014, AJ, 147, 83
Stetson, P. B. 1987, PASP, 99, 191
Stetson, P. B. 1996, PASP, 108, 851
Storrie-Lombardi, L. J., & Dodd, S. R. 2010, Proc. SPIE, 7737, 0
Tody, D. 1986, Proc. SPIE, Vol. 627, 733
van der Marel, N., van Dishoeck, E. F., Bruderer, S., et al. 2013, Sci, 340, 1199
Vrba, F. J., Rydgren, A. E., Chugainov, P. F., Shakovskaia, N. I., & Zak, D. S. 1986, ApJ, 306, 199
Waters, L. B. F. M., & Waelkens, C. 1998, ARA&A, 36, 233
Werner, M. W., Roellig, T. L., Low, F. J., et al. 2004, ApJS, 154, 1
Wilking, B. A., Blackwell, J. H., Mundy, L. G., & Howe, J. E. 1989, ApJ, 345, 257
Wilking, B. A., Bontemps, S., Schuler, R. E., Greene, T. P., & André, P. 2001, ApJ, 551, 357
Wolk, S. J., Moritz Günther, H., & Poppenhaeger, K. 2015, AJ, in press (arXiv:1507.4368)
Wolk, S. J., Rice, T. S., & Aspin, C. 2013, ApJ, 773, 145
Wright, N. J., Drake, J. J., Drew, J. E., et al. 2012, ApJL, 746, L21